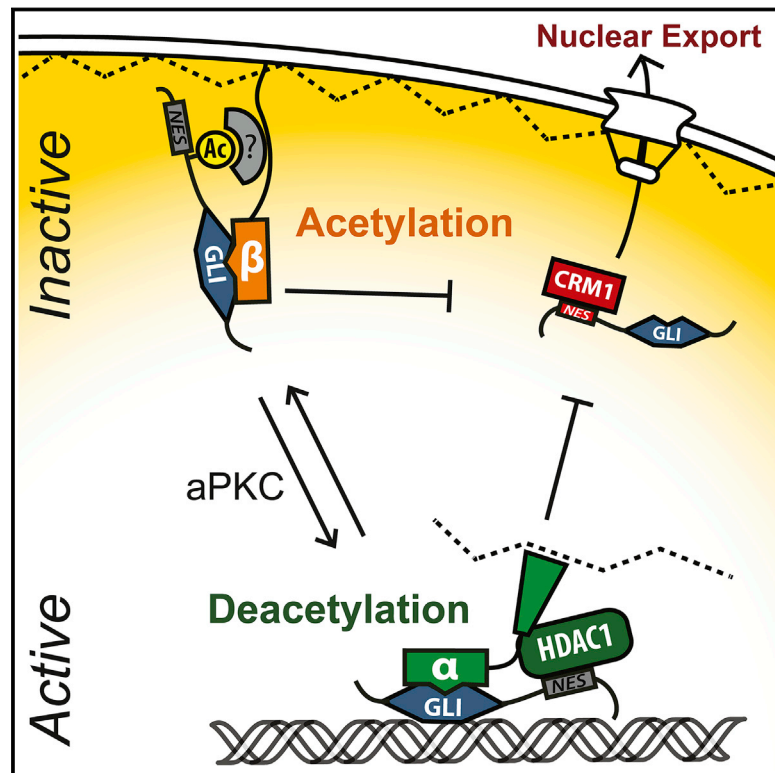# LAP2 Proteins Chaperone GLI1 Movement between the Lamina and Chromatin to Regulate Transcription

Graphical Abstract

Authors

Amar N. Mirza, Siegen A. McKellar, Nicole M. Urman, Alexander S. Brown, Tyler Hollmig, Sumaira Z. Aasi, Anthony E. Oro

Correspondence

oro@stanford.edu

In Brief

A nuclear chaperoning system regulates movement of the transcription factor GLI1 between the nuclear lamina and nucleoplasm to achieve maximal activation.

Highlights

- Acetylated GLI1 accumulates on the lamina via LAP2β to facilitate nuclear retention

- LAP2 isoforms compete to bind GLI1 through a shared LEM-like:zinc finger interaction

- LAP2α forms an activating complex with HDAC1 to deacetylate/activate GLI1

- GLI1:LAP2 interference disrupts Hedgehog signaling in basal cell carcinoma

Article

Cell

LAP2 Proteins Chaperone GLI1 Movement between the Lamina and Chromatin to Regulate Transcription

Amar N. Mirza,[1] Siegen A. McKellar,[1] Nicole M. Urman,[1] Alexander S. Brown,[1] Tyler Hollmig,[1] Sumaira Z. Aasi,[1] and Anthony E. Oro[1,2,*]
[1]Program in Epithelial Biology and Department of Dermatology, Stanford University School of Medicine, Stanford, CA 94305, USA
[2]Lead Contact
*Correspondence: oro@stanford.edu
https://doi.org/10.1016/j.cell.2018.10.054

SUMMARY

Understanding transcription factor navigation through the nucleus remains critical for developing targeted therapeutics. The GLI1 transcription factor must maintain maximal Hedgehog pathway output in basal cell carcinomas (BCCs), and we have previously shown that resistant BCCs increase GLI1 deacetylation through atypical protein kinase Cι/λ (aPKC) and HDAC1. Here we identify a lamina-associated polypeptide 2 (LAP2) isoform-dependent nuclear chaperoning system that regulates GLI1 movement between the nuclear lamina and nucleoplasm to achieve maximal activation. LAP2β forms a two-site interaction with the GLI1 zinc-finger domain and acetylation site, stabilizing an acetylation-dependent reserve on the inner nuclear membrane (INM). By contrast, the nucleoplasmic LAP2α competes with LAP2β for GLI1 while scaffolding HDAC1 to deacetylate the secondary binding site. aPKC functions to promote GLI1 association with LAP2α, promoting egress off the INM. GLI1 intranuclear trafficking by LAP2 isoforms represents a powerful signal amplifier in BCCs with implications for zinc finger-based signal transduction and therapeutics.

INTRODUCTION

Although transcription factors have been intensely studied for gene regulation, an open question remains how they efficiently navigate the dense three-dimensional organization of the eukaryotic nucleus. Rather than a disorganized nucleoplasmic milieu, the nucleus employs a variety of non-membranous compartmentalization mechanisms, including phase separation (Strom et al., 2017), chromatin architecture (Stevens et al., 2017), and spatial segregation to the nuclear lamina (Kind et al., 2015) to precisely control the kinetics of gene regulation.

Collectively termed the nuclear lamina, the inner nuclear membrane (INM) environment harbors heterochromatinized lamina-associated domains, the nuclear pore complex, structural elements such as lamins, and the LEM domain proteins (Chow et al., 2012). The LEM domain proteins, named after the founding members LAP2, Emerin, and MAN1, coordinate the peripheral immobilization and repression of genomic elements and transcription factors directly or indirectly through their canonical interaction partner BANF1 (Brachner and Foisner, 2011; Guilluy et al., 2014; Ho et al., 2013; Lee et al., 2017; Nili et al., 2001; Pan et al., 2005). Among the LEM domain proteins, the lamina-associated polypeptide 2 (LAP2) family contains six splice variants that share an N-terminal LEM-like domain, which confers DNA-binding activity, and a LEM domain, which confers BANF1-binding activity (Cai et al., 2001). LAP2β, the best characterized INM-bound LAP2 isoform, also contains an HDAC3 interaction domain near its transmembrane region, conferring peripheral silencing activity (Poleshko et al., 2017; Somech et al., 2005). LAP2α diverges significantly from other LAP2 isoforms as a nucleoplasmic protein that replaces the transmembrane domain with a unique coiled-coil domain, conferring nucleoplasmic A-type lamin binding activity. LAP2α canonically stabilizes pRb in the nucleoplasm by anchoring it to nucleoplasmic lamins, and LAP2α has been speculated to scaffold HDAC complexes as well (Brachner and Foisner, 2014; Gotic and Foisner, 2010; Naetar et al., 2008).

The GLI family of zinc finger transcription factors controls transcriptional events downstream of the G-protein coupled receptor Smoothened in the Hedgehog (Hh) signaling pathway, and maximal transcriptional output is associated with tumors like basal cell carcinomas (BCCs) (Oro et al., 1997). GLI1 is a pure transcriptional activator and functions in a positive automaintenance loop to sustain the high-level activity needed for tumorigenesis (Hui and Angers, 2011). Accordingly, GLI1 activity is tightly controlled through the regulation of nuclear import and the modulation of protein stability (Gulino et al., 2012). Despite these studies, the mechanism of intranuclear GLI trafficking and regulation remains poorly understood.

A key insight into intranuclear GLI regulation came from the observation that nuclear GLI1 is acetylated at position K518 (AcGLI1) by p300 or CBP, rendering it temporarily inactive. Deacetylation by HDAC1-2 allows GLI1 to associate with chromatin and initiate transcription (Canettieri et al., 2010; Coni et al., 2013). Concordantly, we recently showed, using a drug-repositioning screen, that BCCs resistant to the Smoothened inhibitor vismodegib harbor a transcriptional signature dominated by HDAC1
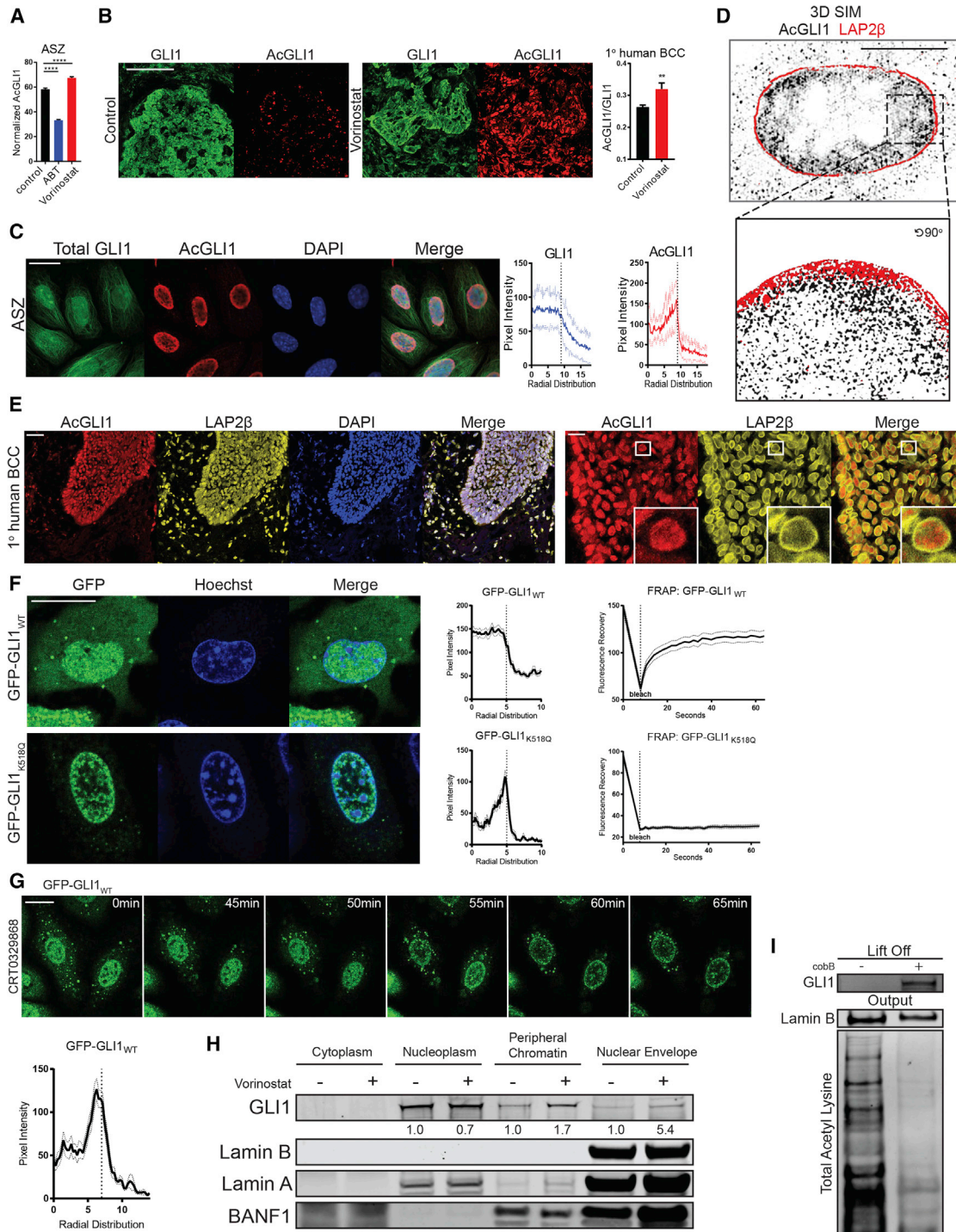
Cell

Figure 1. Acetylated GLI1 Accumulates on the Inner Nuclear Membrane

(A) Quantification of immunostaining of AcGLI1 (normalized to LAP2β) in ASZ cells cultured with vorinostat or ABT (n = 276 (control), 329 (ABT), and 293 (vorinostat) nuclei; ANOVA). See also Figure 2E; additional treatments in Figure S1C.

(B) 1° human BCC cultured *ex vivo* with or without vorinostat (20 μM, 3 hr) immunostained for GLI1 and AcGLI1 (scale bar, 133 μm; n = 10 fields, 2-tailed t test).

(C) Immunofluorescence of total GLI1, AcGLI1, and DAPI in ASZ cells cultured with vorinostat (6 hr, 20 μM) (scale bar, 20 μm, n = 50).

(D) 3D structured illumination microscopy (3D SIM) of ASZ cells cultured with vorinostat (5 hr, 20 μM) (scale bar, 10 μm; AcGLI1, black; LAP2β [inner nuclear membrane [INM] marker], red overlay).

(legend continued on next page)

Cell

activity (Mirza et al., 2017). In addition, we found that the polarity kinase atypical protein kinase C (aPKC), which is frequently hyperactivated in Smoothened inhibitor-resistant BCCs (Atwood et al., 2013), acts predominantly by promoting GLI1:HDAC1 association (Mirza et al., 2017). The convergence of these Smoothened inhibitor resistance mechanisms on the acetylation dynamics of GLI1 necessitates a more refined understanding of the process.

Here we report a LAP2 isoform-dependent nuclear chaperoning system that regulates GLI1 movement between the nuclear lamina and nucleoplasm to achieve maximal activation. By staining with AcGLI1-specific antibodies, we identify a LAP2β-dependent pool of AcGLI1 on the INM that is necessary for nuclear GLI1 accumulation. Utilizing vicinal proteomics, we identify competing LAP2α complexes that promote the deacetylation of GLI1 to control its activation. The BCC drug resistance kinase aPKC functions to shift GLI1 association from LAP2β to LAP2α, promoting egress off of the INM. These LAP2 splice variants utilize a common LEM-like domain to bind the zinc fingers of GLI1, and disruption of this interface represses Hh signaling by interfering with GLI1 intranuclear transport. Further, we identify similar C2H2 zinc-finger proteins that utilize this LEM-like domain interface, suggesting a general zinc-finger scaffolding function for LAP2 proteins.

RESULTS

Acetylated GLI1 Accumulates on the INM

Motivated by the convergence of aPKC and HDAC1 on the deacetylation of GLI1 at residue 518, we raised anti-acetyl K518 GLI1 (AcGLI1) antibodies. AcGLI1 antibodies demonstrated specificity for acetylated GLI1 peptide and full-length protein but not an acetyl-deficient GLI1 mutant (GLI1$_{K518R}$) by immunoblot (Figures S1A–S1C). The AcGLI1 signal dropped following genetic depletion of GLI1 (Figures S1D and S1E). Similarly, the immunofluorescence signal of AcGLI1 decreased in response to p300 or CBP inhibition (ABT) and increased in response to HDAC (vorinostat and entinostat) or aPKC (CRT0329868) inhibition in BCC cells (Figures 1A and S1F). Finally, we confirmed similar increases in immunoreactivity in primary human BCC surgical specimens treated with vorinostat *ex vivo* (Figure 1B), demonstrating the specificity of the antibody.

Surprisingly, immunofluorescence staining of AcGLI1 revealed a distinctive subnuclear gradient of AcGLI1 accumulating on the INM, with lower levels in the nucleoplasm and absent in the cytoplasm, following treatment with HDAC or aPKC inhibitors (Figures 1C and S1F–S1H). By contrast, total GLI1 protein existed in both nuclear and cytoplasmic compartments and uniformly filled the nucleus (Figure 1C). Super-resolution imaging by three-dimensional structured illumination microscopy confirmed the presence of a gradient of AcGLI1 emanating from the INM into the nucleoplasm, which differed from the sharp INM boundary of the INM-anchored LAP2β (Figure 1D). Further, we confirmed the existence of the subnuclear distribution of AcGLI1 in primary human BCCs (Figures 1E and S1I).

To study the redistribution kinetics of GLI1 upon acetylation, we generated doxycycline-inducible GFP-GLI1 in BCC cells for live-cell imaging (Figures S1J and S1K). GFP-GLI1$_{WT}$ in our experiments demonstrated a similar subcellular distribution in living cells as in stained sections (Figure 1F). Remarkably, inhibition of aPKC or HDAC1, which controls the deacetylation of GLI1 (Mirza et al., 2017), resulted in redistribution of GFP-GLI1 from the nucleoplasm to the INM after 1 hr of treatment (Figures 1G and S1L; Videos S1 and S2). Congruently, acetyl-mimetic GFP-GLI1$_{K518Q}$ accumulated on the INM without drug treatment (Figure 1F). Using fluorescence recovery after photobleaching (FRAP), we studied the nuclear mobility of GLI1 in the INM and nucleoplasm. FRAP analysis of nucleoplasmic GFP-GLI1$_{WT}$ indicated a highly mobile population with a recovery half-time of high maximal effect ($t_{1/2}$) of 6 s and a mobile phase of 78%. In contrast, INM-localized GFP-GLI1$_{K518Q}$ demonstrated highly restricted mobility with very little recovery in the timescale tested (Figure 1F; Videos S3 and S4).

We performed subnuclear biochemical fractionation to test acetylation-dependent GLI1 INM association. Previous studies have shown that successive DNase digestions of isolated nuclei liberate fractions corresponding to nucleoplasm (nucleoplasmic A-type lamins), followed by peripheral chromatin (non-integral membrane components such as BANF1) (Kay et al., 1972). In BCC cells, we found the majority of GLI1 in the nucleoplasmic fraction and a minority of GLI1 in the peripheral chromatin fraction, with HDAC inhibition enriching GLI1 in the peripheral chromatin fraction (Figure 1H). To test for acetylation-dependent binding of GLI1 to the INM, we subjected isolated nuclear envelopes to deacetylation *in vitro* by cobB, a non-specific bacterial deacetylase. Crude nuclear envelopes, enriched with GLI1 following HDAC inhibition, released GLI1 in a deacetylation-dependent manner (Figure 1I). Taken together, these data

---

(E) Immunofluorescence staining of primary human BCC frozen sections with affinity-purified AcGLI1 antibody and LAP2β (scale bar, 40 μm [left], 14 μm [right]). Radial distribution is quantitated in Figure S1I.

(F) Confocal live-cell microscopy and fluorescence recovery after photobleaching (FRAP) of ASZ cells expressing GFP-GLI1$_{WT}$ and GFP-GLI1$_{K518Q}$ (center, quantification of the radial distribution of GFP, n = 24 [WT] and 28 [K518Q]) (right, quantification of the FRAP recovery profile following photobleaching [vertical line]; x axis, seconds) (GFP-GLI1$_{WT}$: $t_{1/2}$ = 6 s [4.3–8.7, 95% confidence interval [CI]); mobile fraction = 78% (76–80, 95% CI), n = 24) (GFP-GLI1$_{K518Q}$: $t_{1/2}$ and mobile fraction incalculable because of lack of recovery, n = 28). See also Videos S3 and S4. Confirmation of GFP induction is shown in Figure S1F.

(G) Time-lapse confocal live-cell microscopy of GFP-GLI1$_{WT}$-expressing ASZ cells treated with CRT0329868. Quantification of the radial distribution of GFP-GLI1$_{WT}$ after 1 hr of treatment is shown below (n = 27). See also Videos S1 and S2.

(H) Immunoblot of the indicated fractions for GLI1 and fraction markers following subnuclear fractionation of ASZ cells cultured with or without vorinostat (20 μM, 2 hr).

(I) Immunoblot of sedimented nuclear envelopes (output) and supernatant (lift off) following *in vitro* deacetylation of purified ASZ nuclear envelopes by cobB deacetylase.

All error bars represent SE; **p < 0.01; ****p < 0.0001. Radial distributions: vertical lines indicate the nuclear envelope, x axes represent arbitrary units. See also Figure S1.
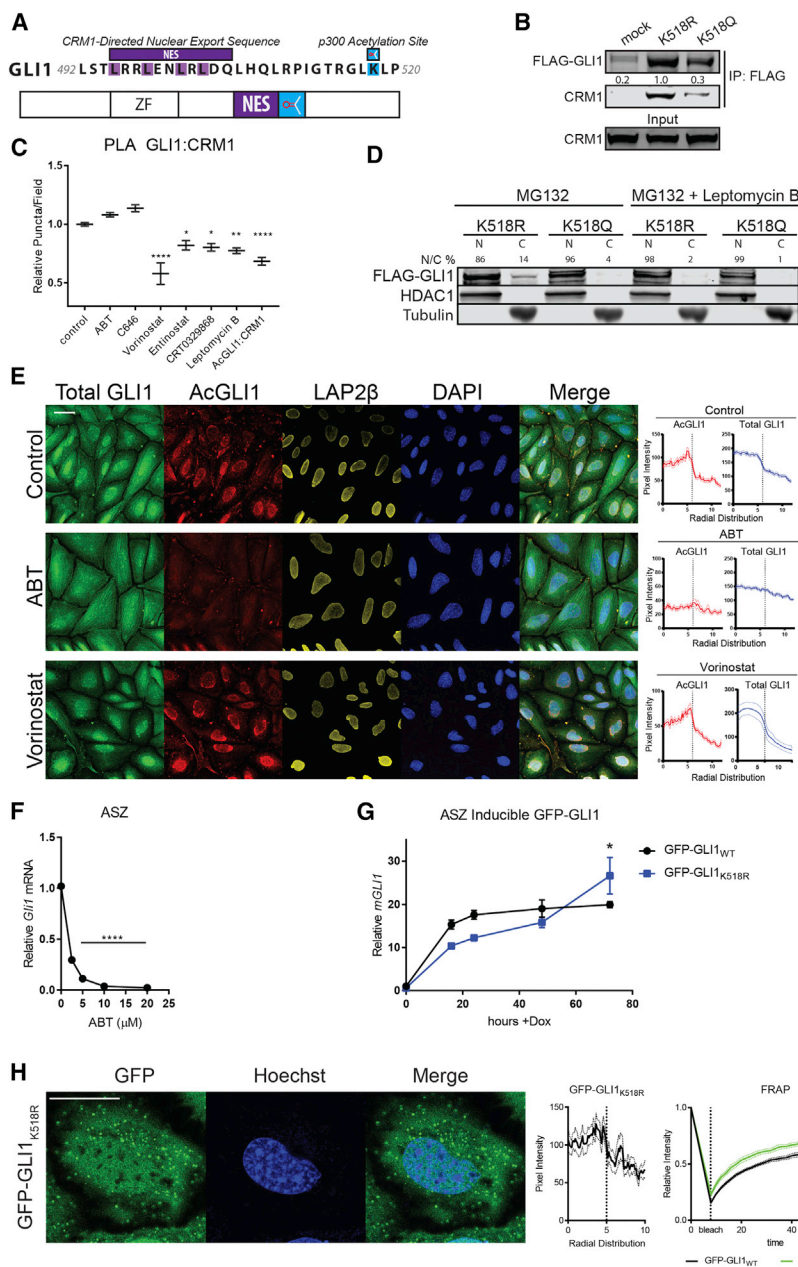
Cell

Figure 2. GLI1 Acetylation Promotes Nuclear Accumulation

(A) Schematic of the CRM1-mediated nuclear export sequence (NES, purple) and acetylation site (blue) on GLI1. ZF, zinc finger.

(B) CoIP of transfected FLAG-GLI1$_{K518R/Q}$ in HEK293T and immunoblot for FLAG and endogenous CRM1.

(C) Proximity ligation assay (PLA) between endogenous GLI1 and CRM1 in ASZ cells cultured with the indicated inhibitors and PLA between AcGLI1 and CRM1. Quantification of puncta per field was normalized to the vehicle control (n = 10 fields, ANOVA).

(D) Nuclear-cytoplasmic fractionation of ASZ cells transfected with FLAG-GLI1$_{K518R/Q}$ and treated with MG132 to visualize cytoplasmic GLI1 with or without leptomycin B.

(E) Immunofluorescence of total GLI1, AcGLI1, DAPI, and LAP2β (INM marker) in ASZ cells treated with vorinostat (20 μM, 3 hr) or ABT (20 μM, 3 hr) (scale bar, 20 μm; radial distribution is quantified on the right, n = 50). Quantification of AcGLI1 is shown in Figure 1B.

(F) qRT-PCR of *GLI1* normalized to *GAPDH* in ASZ cells treated with ABT (16-hr treatment, n = 9, ANOVA).

(G) qRT-PCR of murine *GLI1* normalized to *GAPDH* over an induction time course of GFP-GLI1$_{WT/K518R}$ (n = 9, 2-way ANOVA). Expression data are shown in Figure S2B.

(H) Confocal live-cell microscopy of GFP-GLI1$_{K518R}$ inducible ASZ (scale bar, 20 μm) with quantitation of GFP radial distribution (n = 18) and FRAP (K518R: n = 10, $t_{1/2}$ = 9.7 s [8.4–11.3, 95% CI]; mobile fraction = 72% [70–74, 95% CI]; WT: n = 10, $t_{1/2}$ = 11.0 s [9.6–12.8, 95% CI], mobile fraction = 63.9% [62.3–65.2, 95% CI], 2-way ANOVA). All error bars represent SE; error bars were omitted when smaller than the width of the associated data point symbol. ns, not significant; *p < 0.05; **p < 0.01; ***p < 0.001; ****p < 0.0001. Radial distributions: vertical lines indicate nuclear envelopes, x axes represent arbitrary units. See also Figure S2.

demonstrate a dynamic acetylation-dependent interaction between GLI1 and the INM.

GLI1 Acetylation Promotes Nuclear Accumulation

High-resolution imaging and fractionation indicated that AcGLI1 localizes exclusively in the nucleus. Previous studies have shown that GLI1 nuclear occupancy depends on its interaction with the CRM1 nuclear export machinery (Kogerman et al., 1999). Because of the proximity of the GLI1 acetylation site (K518) to its CRM1-dependent nuclear export sequence (495–503), we hypothesized that acetylation of GLI1 prevents nuclear export (Figure 2A). Indeed, co-immunoprecipitation (coIP) of GLI1$_{K518Q}$ reflected impaired CRM1 binding compared with GLI1$_{K518R/WT}$

(Figures 2B and S2A). In addition, proximity ligation assays (PLAs) between endogenous GLI1 and CRM1 in BCC cells demonstrated an interaction enhanced by p300 or CBP inhibition (ABT and C646) and depressed by HDAC inhibition (vorinostat and entinostat), aPKC inhibition (CRT0329868), or CRM1 inhibition (leptomycin B). Congruently, a PLA between AcGLI1 and CRM1 demonstrated weak interaction (Figure 2C). We conclude that GLI1 acetylation disrupts CRM1 binding.

To determine whether CRM1 binding disruption correlates with impairment of GLI1 nuclear export, we performed subcellular fractionation of GLI1$_{K518Q}$ and GLI1$_{K518R}$. In BCC cells, GLI1$_{K518R}$ demonstrated a minor cytoplasmic fraction that is sensitive to leptomycin B treatment, indicating dependence on nuclear export. This export-dependent fraction was absent in GLI1$_{K518Q}$, a result consistent in NIH 3T3 cells as well (Figures
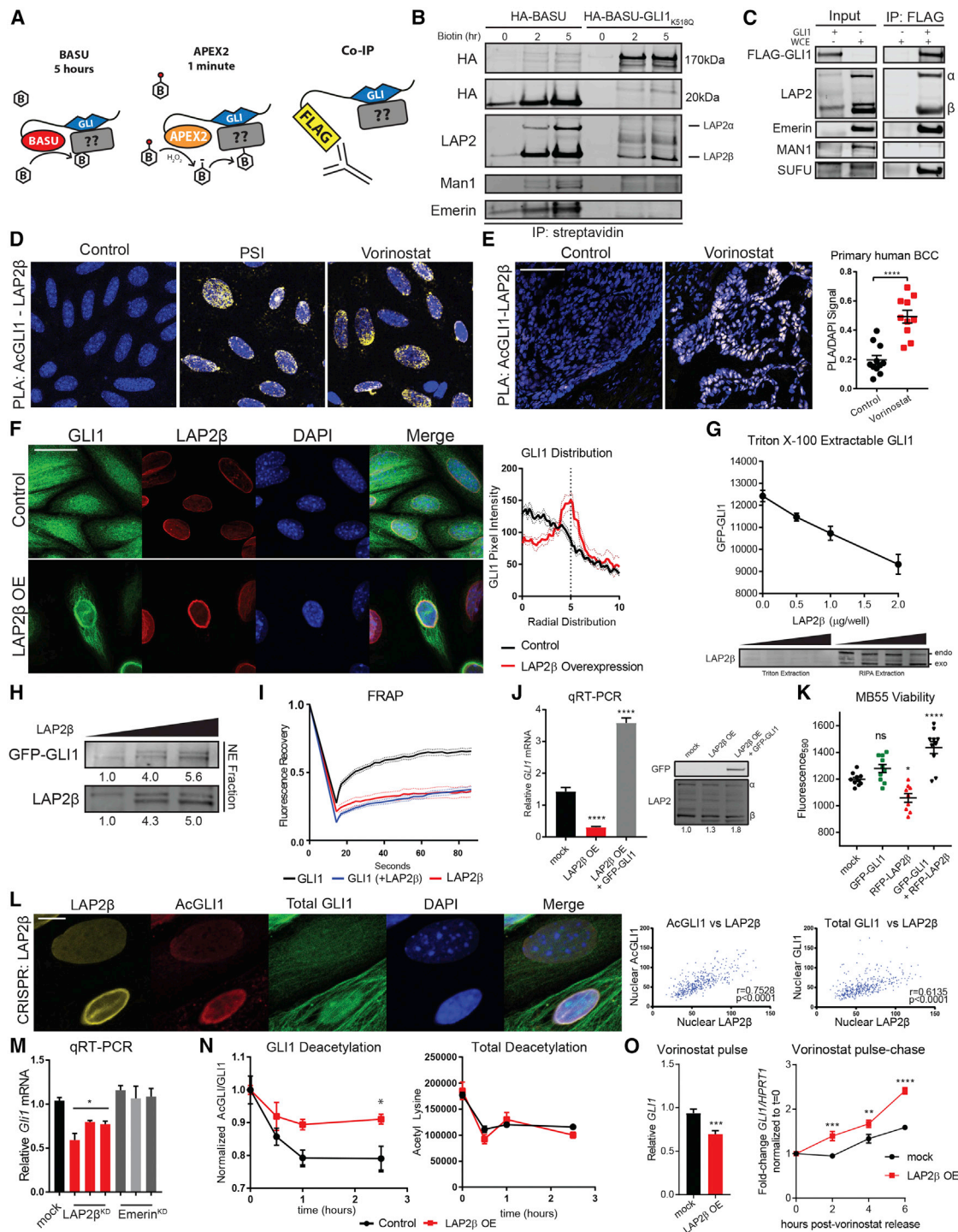
Figure 3. LAP2β Anchors AcGLI1 to the INM

(A) Schematic of the three orthogonal protein-protein interaction techniques used ("B" represents biotin).

(B) Streptavidin pull-down and immunoblot with the indicated antibodies of lysates in HEK293T cells following vicinal labeling with stably expressing hemagglutinin (HA)-BASU (20 kDa) or HA-BASU-GLI1$_{K518Q}$ (170 kDa).

(C) CoIP of *in-vitro*-translated FLAG-GLI1 following incubation in HEK293T whole-cell extract (WCE).

(D) PLA between AcGLI1 and LAP2β in ASZ cells following the indicated drug treatments (scale bar, 20 μm; yellow puncta indicate interaction). Quantification is shown in Figure S3E.

(legend continued on next page)

Cell

2D and S2B). Furthermore, inhibition of endogenous GLI1 acetylation by ABT redistributed GLI1 into the cytoplasm, whereas inhibition of deacetylation by vorinostat retained GLI1 in the nucleus by immunofluorescence (Figure 2E).

To determine the transcriptional effects of GLI1 acetylation, we measured autotranscription of *GLI1*, a well-established endogenous pathway target gene. Inhibition of p300 and CBP impaired GLI1 transcriptional output (Figure 2F), consistent with the lack of nuclear accumulation. Careful titration of $GLI1_{WT}$ and $GLI1_{K518R}$ protein by doxycycline induction over time indicated that $GLI1_{WT}$ demonstrates greater transcriptional potency than $GLI1_{K518R}$ at lower protein levels (Figures 2G and S2C). $GLI1_{K518R}$ required high levels of protein to overcome its nuclear export disadvantage before the effects of removing the inhibitory effect of GLI1 acetylation dominated (Figure S2D). Correspondingly, $GFP-GLI1_{K518R}$ failed to accumulate in the nucleus appropriately in living cells and displayed enhanced mobility by FRAP in BCC cells (Figure 2H). Taken together, GLI1 acetylation acts as a signal amplifier for maximal activity by promoting nuclear accumulation through the creation of a dynamic but inactive reserve of protein on the INM.

LAP2β Anchors AcGLI1 to the INM

To identify candidate INM components that bind GLI1, we initially compared changes in expression of the LEM domain proteins, LINC complex, and nuclear pore complex by RNA sequencing of human BCC-normal skin pairs and found specific overexpression of the LEM domain protein LAP2-TMPO (Figure S3A). Through examination of the Human Protein Atlas Database, we compared BCCs with squamous cell carcinomas and observed similar overexpression of LAP2 (Figure S3B). In addition, we performed a candidate vicinal proteomics screen employing three protein-protein interaction technologies with GLI1 (Figure 3A) and, in each case, identified LAP2. *Bacillus subtilis*-adapted biotin ligase (BASU) (Ramanathan et al., 2018)

$GLI1_{K518Q}$ fusions specifically labeled the INM LAP2 isoform LAP2β to the exclusion of the INM proteins Man1 and Emerin and the non-INM LAP2 isoform LAP2α (Figure 3B). Using an orthogonal vicinal labeling scheme, $APEX2-GLI1_{WT}$ fusions also labeled LAP2β upon GLI1 acetylation by HDAC inhibition (Figures S3C and S3D).

CoIP of $FLAG-GLI1_{WT}$ demonstrated physical interaction between GLI1 and LAP2β in addition to Emerin, LAP2α (discussed below), and the canonical GLI1 interactor suppressor of fused (SUFU) (Figure 3C). Among the INM interactors, only LAP2β displayed GLI1 acetylation-dependent binding affinity. CoIP of *in-vitro*-translated FLAG-GLI1 after incubation with HEK293T whole-cell extract demonstrated a robust physical interaction with LAP2β that weakened with acetyl-deficient $GLI1_{K518R}$ (Figure S3E). Importantly, Emerin failed to demonstrate similar acetylation-dependent binding (Figure S3F). Similarly, the PLA signal between endogenous AcGLI1 and LAP2β amplified in response to HDAC (vorinostat) or aPKC (PSI) inhibition in BCC cells, localizing appropriately to the INM (Figures 3D and S3G). The acetylation-dependent interaction could also be detected in primary human BCCs because tumors treated with vorinostat *ex vivo* demonstrated a robust AcGLI1:LAP2β PLA signal (Figure 3E). We conclude that AcGLI1 interacts with LAP2β on the INM.

Next, we assayed for LAP2β-dependent peripheral sequestration of GLI1 using gain-of-function assays. LAP2β overexpression redistributed GLI1 protein to the INM by immunofluorescence (Figures 3F and S3H) whereas Emerin overexpression did not (Figure S3I). Correspondingly, Triton X-100-extractable GLI1 decreased linearly with LAP2β overexpression (Figure 3G), and GLI1 abundance in the nuclear envelope fraction increased linearly with LAP2β overexpression (Figure 3H). Finally, FRAP analysis of INM-localized GLI1 upon LAP2β overexpression demonstrated a greatly reduced mobile fraction compared with nucleoplasmic GLI1, mirroring the mobility of LAP2β alone (Figures 3I and S3J). These data indicate that LAP2β

(E) PLA between AcGLI1 and LAP2β in 1° human BCCs cultured *ex vivo* with vorinostat (scale bar, 80 μm; a yellow signal indicates interaction; n = 10 fields; 2-tailed t test).

(F) Immunofluorescence of GLI1 and LAP2β in ASZ cells following LAP2β overexpression (OE) (scale bar, 20 μm). Radial distribution was quantified (the vertical line indicates the nuclear envelope; n = 30; x axis, arbitrary units).

(G) Quantitation of a dot blot of supernatant from GFP-GLI1-inducible ASZ cells transfected with a gradient of LAP2β followed by 1% Triton X-100 extraction (n = 9). Shown is a western blot of initial Triton X-100 extraction and subsequent RIPA extraction included for LAP2β. Exogenous (exo; *R. norvegicus*) and endogenous (endo) LAP2β are indicated by arrows.

(H) GFP-GLI1-inducible ASZ cells transfected with a gradient of LAP2β, followed by nuclear envelope fractionation and immunoblot.

(I) FRAP profile of GFP-GLI1 and RFP-LAP2β co-transfected in HEK293T cells (n = 16 [GFP-GLI1], 15 [RFP- LAP2β], or 7 [both]) (GFP-GLI1: $t_{1/2}$ = 8.5 s [7–10, 95% CI]; mobile fraction = 65% [64–67, 95% CI]) (RFP-LAP2β: $t_{1/2}$ = 11.9 s [5–48, 95% CI]; mobile fraction = 36% [33–47, 95% CI]) (RFP-LAP2β and GFPGLI1: $t_{1/2}$ = 18.9 s [13–32, 95% CI]; mobile fraction = 39% [36–46, 95% CI]).

(J) qRT-PCR of murine *GLI1* transcript normalized to *GAPDH* following LAP2β OE and GFP-GLI1 (*Homo sapiens*) induction in ASZ cells (n = 9, ANOVA). Shown is a western blot with quantitation of LAP2β normalized to LAP2α.

(K) MB55 cells transfected with the indicated plasmids were assayed for viability by CellTiter-Blue (n = 10, ANOVA).

(L) Heterogeneous depletion of LAP2β by CRISPR-Cas9 targeting exon 6 of *TMPO* in ASZ cells followed by immunofluorescence (scale bar, 20 μm) (n = 398 nuclei, Pearson correlation coefficients). Supportive quantitation is shown in Figure S4D. Cells with varying levels of LAP2β were included as an internal control.

(M) siRNA knockdown of LEM domain proteins using three unique siRNAs per target in ASZ cells, followed by qRT-PCR of *GLI1* and *GAPDH* (n = 9, ANOVA). Supportive qRT-PCR and immunoblots are shown in Figures S4E and S4F.

(N) Vorinostat pulse-chase in ASZ cells transfected with empty vector or LAP2β, followed by dot blot of AcGLI1, GLI1, and total acetylated lysine (n = 9, 2-way ANOVA). Supportive quantification of LAP2β is shown in Figure S4G.

(O) qRT-PCR of the *GLI1* transcript following vorinostat treatment for 3 hr with LAP2β OE (left, n = 9, 2-tailed t test) and kinetics of transcriptional recovery following vorinostat withdrawal (right, n = 9, 2-way ANOVA, each condition normalized to t = 0). An associated immunoblot is shown in Figure S4H.

Error bars represent SE. Error bars were omitted when smaller than the width of the associated data point symbol. *p < 0.05, **p < 0.01, ***p < 0.001, ****p < 0.0001. See also Figures S3 and S4.
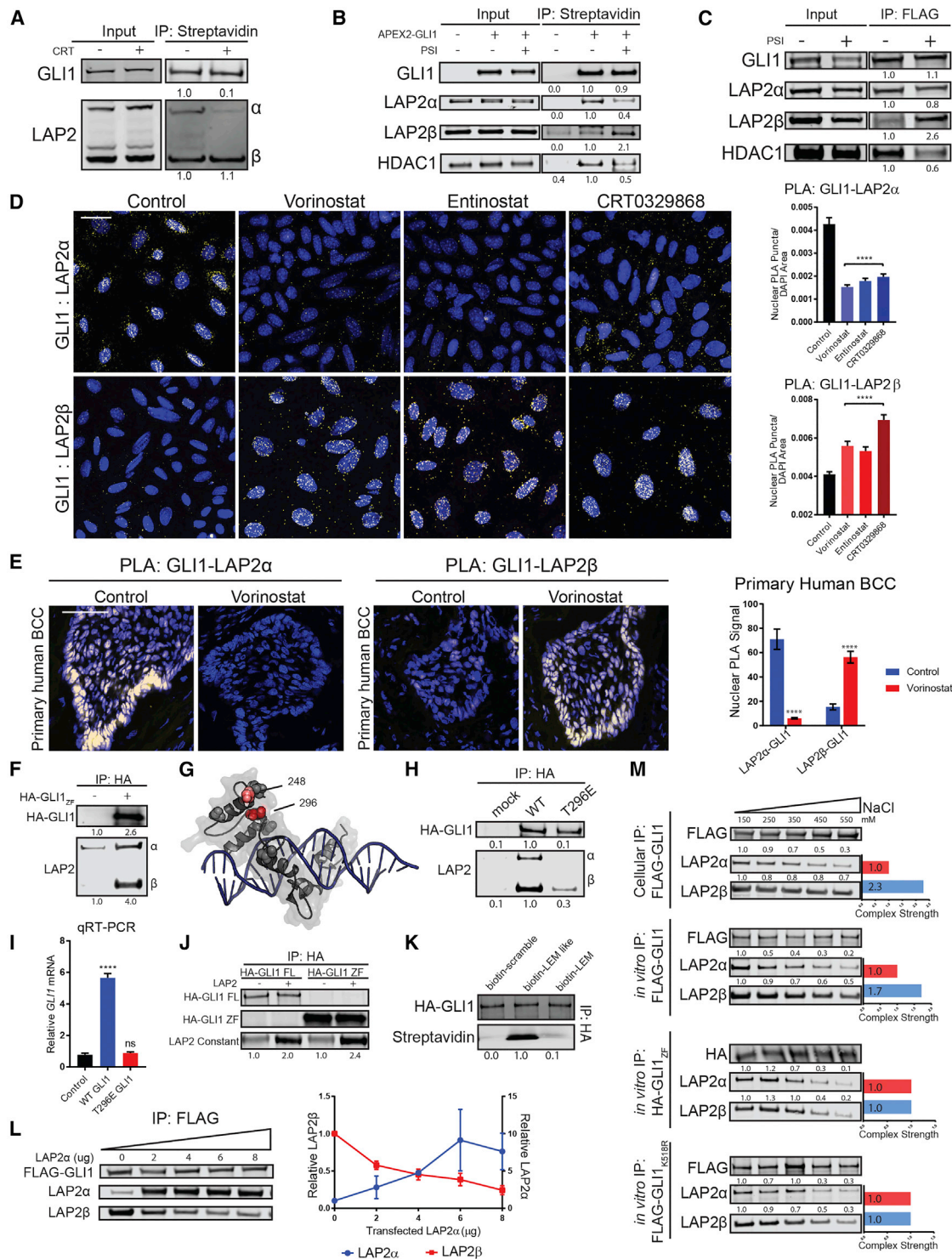
Cell

Figure 4. GLI1 Switches between LAP2 Isoforms upon Acetylation

(A) BASU-GLI1 vicinal labeling in ASZ cells, followed by streptavidin pulldown with or without CRT0329868 (CRT) (+biotin, +CRT, 5 hr).

(B) APEX2-GLI1 vicinal labeling in ASZ cells, followed by streptavidin pulldown with or without PSI.

(C) CoIP of FLAG-GLI1 in ASZ cells with or without PSI, followed by immunoblot.

(D) PLA between total GLI1 and LAP2α (top) or LAP2β (bottom) in ASZ cells treated with the indicated inhibitors for 2 hr (scale bar, 20 μm, n = 10 fields, ANOVA).

(E) PLA between total GLI1 and LAP2α (left) or LAP2β (right) in 1° human BCCs treated with vorinostat *ex vivo* (scale bar, 66 μm, n = 10 fields, ANOVA).

(F) CoIP of *in-vitro*-translated HA-GLI1 zinc-finger domain (HA-GLI1[ZF]) from WCE. Inputs are shown in Figure S5B.

(legend continued on next page)

Cell

overexpression is sufficient to sequester GLI1 to the nuclear lamina. Further, LAP2β overexpression was associated with inhibition of Hh pathway output, which could be rescued by exogenous GLI1 expression (Figures 3J and S3K). As a control, Emerin overexpression had no effect on GLI1 activity (Figure S3L). Concordantly, LAP2β overexpression inhibited the viability of an Hh-dependent cell line, which could be reversed by GLI1 overexpression (Figure 3K). We conclude that LAP2β sequesters GLI1 to the INM, which inhibits transcriptional output.

Although LAP2β overexpression reveals a repressive function on GLI1, genetic depletion of LAP2β demonstrated an additional positive role it plays in GLI1 activity. Small interfering RNA (siRNA)-mediated LAP2β knockdown resulted in loss of AcGLI1 (Figure S3M). Similarly, LAP2β isoform deletion by CRISPR-Cas9-mediated disruption of *TMPO* (exon 6) also resulted in loss of AcGLI1 in addition to total GLI1 protein in ASZ and NIH 3T3 cells (Figures 3L, S3N, and S4A; Table S1). To decouple GLI1 abundance from Hh pathway output, we depleted LAP2β by CRISPR-Cas9 in the doxycycline-inducible GFP-GLI1 stable line. LAP2β depletion again correlated with loss of AcGLI1 and GFP-GLI1, indicating that GLI1 protein stability decreased following LAP2β depletion (Figure S4B). An immunoblot indicated that this loss of GFP-GLI1 stability could be reversed by exogenous LAP2β expression, proteasome inhibition, or nuclear export inhibition (Figure S4C). Notably, proteasome inhibition resulted in cytoplasmic accumulation of GFP-GLI1, and nuclear export inhibition alone was sufficient to rescue nuclear GFP-GLI1 accumulation (Figure S4D). These data indicate that LAP2β is necessary for the nuclear accumulation of GLI1, revealing that the lamina compartment antagonizes nuclear export and subsequent degradation of GLI1. Congruently, knockdown of LAP2β, but not Man1 or Emerin, resulted in decreased Hh target gene transcription (Figures 3M, S4E, and S4F).

Because AcGLI1 accumulated on the INM through an interaction with LAP2β, and LAP2β knockdown decreased AcGLI1 abundance, we hypothesized that LAP2β overexpression should increase the ratio of AcGLI1 to GLI1. LAP2β overexpression produced a greater AcGLI1 to GLI1 resting ratio without impacting global lysine deacetylation or the rate of GLI1 deacetylation ($t_{1/2}$) in a vorinostat pulse-chase experiment (Figures 3N and S4G). Assaying the functional significance of this LAP2β-generated AcGLI1 buffer, we performed qPCR of the *GLI1* transcript during a vorinostat pulse-chase in the context of LAP2β overexpression. Although LAP2β overexpression inhibited GLI1 activity at steady state, LAP2β overexpression resulted in faster recovery from HDAC inhibitor release (Figures 3O and S4H). The synthesis of these results indicates that LAP2β plays a dual role in GLI1 activity. LAP2β sequesters GLI1 to the nuclear periphery in an inactive complex, but this complex facilitates the subsequent activation of GLI1 by antagonizing nuclear export and facilitating rapid transcriptional recovery.

Because LAP2β has been implicated in the peripheral positioning of genomic loci during development (Poleshko et al., 2017), we investigated whether GLI-binding loci localize to the lamina upon GLI1 acetylation. Because of the technical challenges of chromatin immunoprecipitation with the nuclear lamina, we leveraged the vicinal genomic labeling technology of DNA adenine methyltransferase identification (DamID) (Kind et al., 2015). Dam-LAP2β genomic labeling indicated that GLI1-binding loci do not enrich on the nuclear envelope either at steady state or upon GLI1 hyperacetylation following HDAC or aPKC inhibitor treatment (Figures S4I and S4J). These data indicate that lamina-associated AcGLI1 does not bind DNA.

GLI1 Switches between LAP2 Isoforms upon Acetylation
During the course of investigating GLI1's association with LAP2β, we observed that GLI1 also associated with LAP2α, a nucleoplasmic LAP2 isoform, in a deacetylation or activation-dependent manner. Although also a product of the *TMPO* gene, LAP2α replaces its transmembrane domain with a unique coiled-coil domain, allowing nucleoplasmic positioning. Using a pan-LAP2 antibody to observe both isoforms, BASU-GLI1$_{WT}$ robustly labeled both isoforms during maximal Hh pathway activation. By contrast, with aPKC inhibition and the resulting GLI1 acetylation, BASU-GLI1$_{WT}$ primarily labeled LAP2β (Figure 4A). Similar results were seen using the APEX2-GLI1$_{WT}$ labeling approach (Figure 4B). Finally, coIP of FLAG-GLI1$_{WT}$ and subsequent blotting for LAP2 isoforms revealed the LAP2α-to-LAP2β isoform switch upon aPKC inhibition and HDAC1 dissociation (Figure 4C).

We confirmed LAP2α-to-LAP2β isoform switching with endogenous proteins by PLA, using multiple drugs to induce GLI1 acetylation. In BCC cells, the GLI1-LAP2α PLA signal can be eliminated by HDAC (vorinostat and entinostat) or aPKC (CRT0329868) inhibition. Concurrently, these same perturbations enhanced the GLI1-LAP2β PLA signal (Figure 4D). To confirm the switching in primary tissues, we interrogated primary

(G) LAP2-binding mutants mapped onto the GLI1:DNA crystal structure (PDB: 2GLI). Mutations that inhibit (red) or are permissive of (gray) LAP2 binding are illustrated as spheres. CoIP is shown in Figure S5C.

(H) CoIP of HA-GLI1$_{WT/T296E}$ transfected into HEK293T cells, followed by immunoblot of endogenous LAP2. Inputs are shown in Figure S5D.

(I) qRT-PCR of *GLI1* and *GAPDH* following transfection of GLI1$_{WT/T296E}$ into NIH 3T3 cells (n = 9, ANOVA). An associated immunoblot is shown in Figure S5E.

(J) CoIP of full-length GLI1 (GLI1 FL) or zinc-finger domain GLI1 (GLI1 ZF) with recombinant LAP2 constant region (−/+ indicate the addition of LAP2 peptide). Input is shown in Figure S5F.

(K) CoIP of wheat germ cell extract *in-vitro*-translated HA-GLI1 with chemically synthesized biotin-LEM-like (residues 5–48), biotin-LEM (residues 109–153) or biotin-scrambled LEM-like domains. Associated inputs and the saturation binding experiment are shown in Figures S5G and S5H.

(L) CoIP of FLAG-GLI1 co-transfected into HEK293T cells with a gradient of LAP2α, followed by immunoblot for total LAP2 (n = 3). Input and reciprocal immunoprecipitation (IP) are shown in Figures S5I and S5J.

(M) GLI1 transfected in HEK293T cells (top, cellular IP) or *in-vitro*-translated and incubated in WCE (center and bottom, *in vitro* IP) with the indicated mutations or truncations co-immunoprecipitated with the associated epitope tag. The IP was washed over a gradient of high-salt conditions prior to immunoblotting. *Complex strength* $= -slope(x)^{-1}/-slope(\propto)^{-1}$

Error bars represent SE. Error bars were omitted when smaller than the width of associated data point symbol. ****p < 0.0001. See also Figure S5.
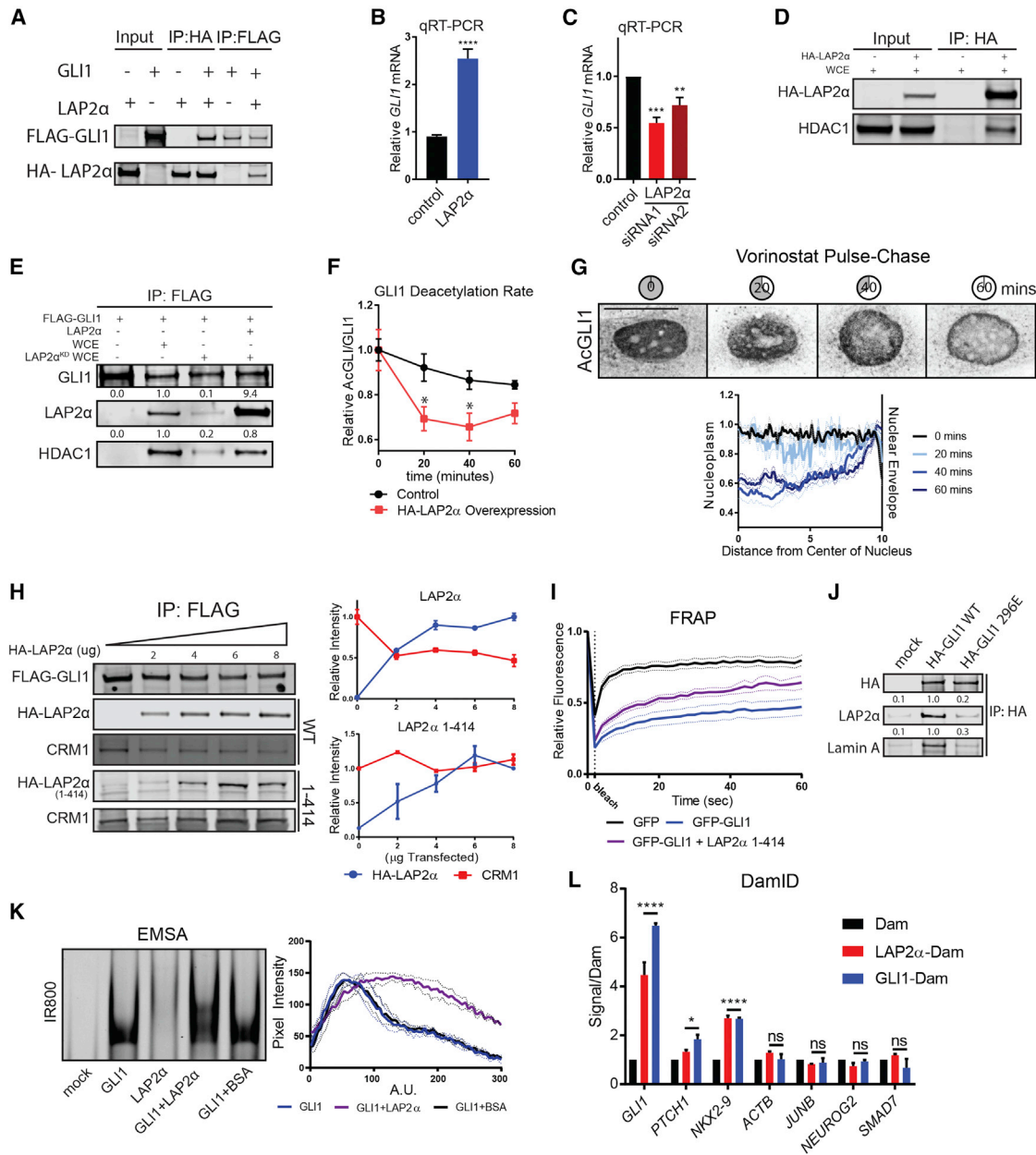
Cell

Figure 5. LAP2α Forms a Nucleoplasmic Activating Complex that Protects Deacetylated GLI1

(A) Reciprocal coIP of *in-vitro*-translated FLAG-GLI1 and HA-LAP2α.

(B and C) qRT-PCR of *GLI1* and *GAPDH* following LAP2α transfection (B) or siRNA knockdown with two unique targeting sequences (C) in ASZ cells (n = 9, ANOVA). Associated immunoblots are shown in Figures S6C and S6D.

(D) CoIP of *in-vitro*-translated HA-LAP2α following incubation in WCE from HEK293T cells.

(E) CoIP of *in-vitro*-translated FLAG-GLI1 from HEK293T WCE or WCE depleted of LAP2α (LAP2α^{KD} WCE) by siRNA. Rescue was performed with *in-vitro*-translated LAP2α. Input is shown in Figure S6F.

(F) Vorinostat pulse-chase in ASZ cells transfected with empty vector or LAP2α, followed by dot blot of AcGLI1 and GLI1 (n = 9, 2-way ANOVA). Supportive quantification of HA-LAP2α is shown in Figure S6G.

(G) Immunofluorescence staining of AcGLI1 in ASZ cells during the chase of a vorinostat pulse-chase. Shown are quantification (top) of nuclear AcGLI1 distribution (n = 30) and representative images (bottom; scale bar, 20 μm).

(H) CoIP of FLAG-GLI1 with HA-LAP2α or HA-LAP2α$_{1-414}$ co-transfected into HEK293T cells. For clarity, a single representative FLAG immunoblot is included. Quantification is included on the right (n = 2). Inputs for associated immunoblots are included in Figure S6H.

(I) FRAP profile of GFP, GFP-GLI1, or GFP-GLI1 + LAP2α$_{1-414}$ co-transfected in HEK293T cells (n = 13 [GFP], 10 [GFP-GLI1], and 12 [GFP-GLI1 + LAP2α$_{1-414}$]; error bars represent SE) (GFP: $t_{1/2}$ = 2.3 s [1.5–3.5, 95% CI]; mobile fraction = 78% [76–79, 95% CI]) (GFP-GLI1: $t_{1/2}$ = 9.6 s [4.8–26, 95% CI]; mobile fraction = 46%

(legend continued on next page)

Cell

human BCCs upon HDAC inhibition and observed similar LAP2α-to-LAP2β PLA signal switching (Figure 4E). We conclude that acetylation regulates GLI1 binding between LAP2 isoforms, with active deacetylated GLI1 associating with LAP2α in the nucleoplasm and inactivated AcGLI1 associating with LAP2β on the INM.

LAP2 Proteins Compete to Bind the Zinc Fingers of GLI1

To identify the interaction surface for the GLI1:LAP2 interaction, we performed coIP experiments with a series of GLI1 and LAP2 mutants. *In-vitro*-translated LAP2α pulled down recombinant fragments of GLI1 that correspond to the zinc-finger domain (Figure S5A). CoIP of the *in-vitro*-translated GLI1 zinc-finger domain from whole-cell extract demonstrated an interaction with both LAP2 isoforms (Figures 4F and S5B). Scanning mutagenesis of the GLI1 zinc-finger domain identified two mutants, $GLI1_{T296E}$ and $GLI1_{S248E}$, which failed to interact with both LAP2 isoforms in a cell-free system (Figures 4G and S5C). CoIP of $GLI1_{T296E}$ from HEK293T cells also lacked robust LAP2 binding (Figures 4H and S5D). Finally, $GLI1_{T296E}$ lacked the ability to induce Hh target gene transcription (Figures 4I and S5E). We conclude that LAP2 proteins share a common binding site between the first and second zinc finger of GLI1.

Because the LAP2 isoforms contain a common N-terminal LAP2 constant region, we hypothesized that it mediates the pan-LAP2:GLI1 interaction. CoIP of the recombinant LAP2 constant region with *in-vitro*-translated full-length and zinc-finger domain GLI1 recapitulated the strong interaction (Figures 4J and S5F). The LAP2 constant region consists of a LEM and LEM-like domain. The purified LEM-like domain strongly associated with GLI1 compared with the LEM domain or a scrambled LEM-like domain (Figures 4K and S5G). A saturation binding experiment by coIP of wheat germ cell extract *in-vitro*-translated GLI1 over a gradient of chemically synthesized LEM-like domain indicated an interaction with an apparent K_D of 8 μM (Figure S5H). If both LAP2 isoforms bind to a common region on GLI1, then one would expect competitive binding between LAP2α and LAP2β on GLI1. Indeed, coIP of GLI1 in HEK293T cells overexpressing LAP2α showed that LAP2α competed off LAP2β (Figures 4L and S5I). Conversely, LAP2β overexpression similarly competed off LAP2α (Figure S5J), supporting direct competition between the two isoforms for GLI1.

Given a common binding domain, we investigated how acetylation of GLI1 affects isoform selection using a gradient of high-salt washes. CoIP of GLI1 from HEK293T cells indicated that LAP2β forms a more robust interaction with GLI1 than LAP2α (Figure 4M, top). Similarly, coIP of *in-vitro*-translated GLI1 from HEK293T whole-cell extract yielded a more robust LAP2β com-

plex (Figure 4M, second from the top). By contrast, the *in-vitro*-translated GLI1 zinc-finger domain formed LAP2 complexes of similar strength, revealing a secondary binding site outside of the zinc-finger domain that determines the LAP2β preference (Figure 4M, third from the top). Highlighting the importance of GLI1 acetylation, *in-vitro*-translated, full-length acetyl-deficient $GLI1_{K518R}$ bound LAP2 complexes with similar strength (Figure 4M, bottom). Taken together, LAP2 proteins share an interaction surface between their LEM-like domain and the first and second zinc fingers of GLI1. LAP2β forms a second site interaction with GLI1 at its acetylation site, conferring acetylation-dependent binding strength (Figure S5K). Notably, LAP2β no longer associated with GLI1 in an acetylation-dependent manner when the proteins were generated in a wheat germ cell extract *in vitro* translation system, indicating the requirement of other molecular factors for full binding (Figure S5L).

LAP2α Forms a Nucleoplasmic Activating Complex that Protects Deacetylated GLI1

Pathway activation and GLI1 deacetylation increased GLI1 association with LAP2α, suggesting that LAP2α forms an activating complex with GLI1. Indeed, *in-vitro*-translated GLI1 and LAP2α interacted reciprocally by coIP, forming a complex that withstood stringent high-salt conditions (Figures 5A and S6A). Furthermore, transfected LAP2α formed a specific complex with GLI1 but not with three abundant nuclear transcription factors: E2F-1, Fos, and HNF1α (Figure S6B). Consistent with an activating role, overexpression of LAP2α resulted in Hh pathway hyperactivation (Figures 5B and S6C), whereas knockdown depressed Hh output (Figures 5C and S6D).

We next investigated LAP2α-associated factors that promote GLI1 binding and activation. Interestingly, previous studies have speculated that LAP2α can scaffold HDAC proteins (Gotic and Foisner, 2010; Zastrow et al., 2004), so we assessed whether LAP2α recruits HDAC1 to GLI1. CoIP of LAP2α in HEK293T cells in the presence of transfected GLI1 demonstrated robust HDAC1 association (Figure S6B). Further, *in-vitro*-translated LAP2α still bound to HDAC1 even in wild-type HEK293T whole-cell extract, which lacks endogenous GLI1 protein (Figure 5D). The interaction could be observed reciprocally because coIP of *in-vitro*-translated HDAC1 pulls down LAP2α, but the full HDAC1:LAP2α:GLI1 complex failed to form *in vitro*, indicating the requirement for additional factors (Figure S6E). To confirm that LAP2α scaffolds HDAC1 to GLI1, we generated whole-cell extract depleted of LAP2α by siRNA silencing (Figure S6F). Although coIP of *in-vitro*-translated GLI1 mixed with wild-type whole-cell extract revealed interactions with both LAP2α and HDAC1, coIP from LAP2α-depleted whole-cell extract lacked

[42–55, 95% CI]) (GFP-GLI1 + $LAP2α_{1–414}$: $t_{1/2}$ = 10.5 s [7.5–15, 95% CI]; mobile fraction = 63% [60–67, 95% CI]). Associated immunoblots are shown in Figure S6J.

(J) CoIP of $HA-GLI1_{WT/T296E}$ transfected into HEK293T cells.

(K) Electrophoretic mobility shift assay (EMSA) of the recombinant GST-GLI1 zinc-finger domain with the addition of wheat germ cell extract *in-vitro*-translated LAP2α or BSA. Supershifting is quantified on the right (n = 7, dotted lines indicate SE). Associated quantitation of total signal is shown in Figure S6K.

(L) Vicinal genomic labeling in NIH 3T3 cells by DamID, Damid-GLI1, and Damid-LAP2α, followed by isolation of labeled regions and qPCR of canonical GLI1 binding sites and non-GLI sites (n = 9, ANOVA). Associated DamID validation data are shown in Figures S6L and S6M.

Error bars represent SE. Error bars were omitted when smaller than the width of the associated data point symbol. *p < 0.05, **p < 0.01, ***p < 0.001, ****p < 0.0001. See also Figure S6.
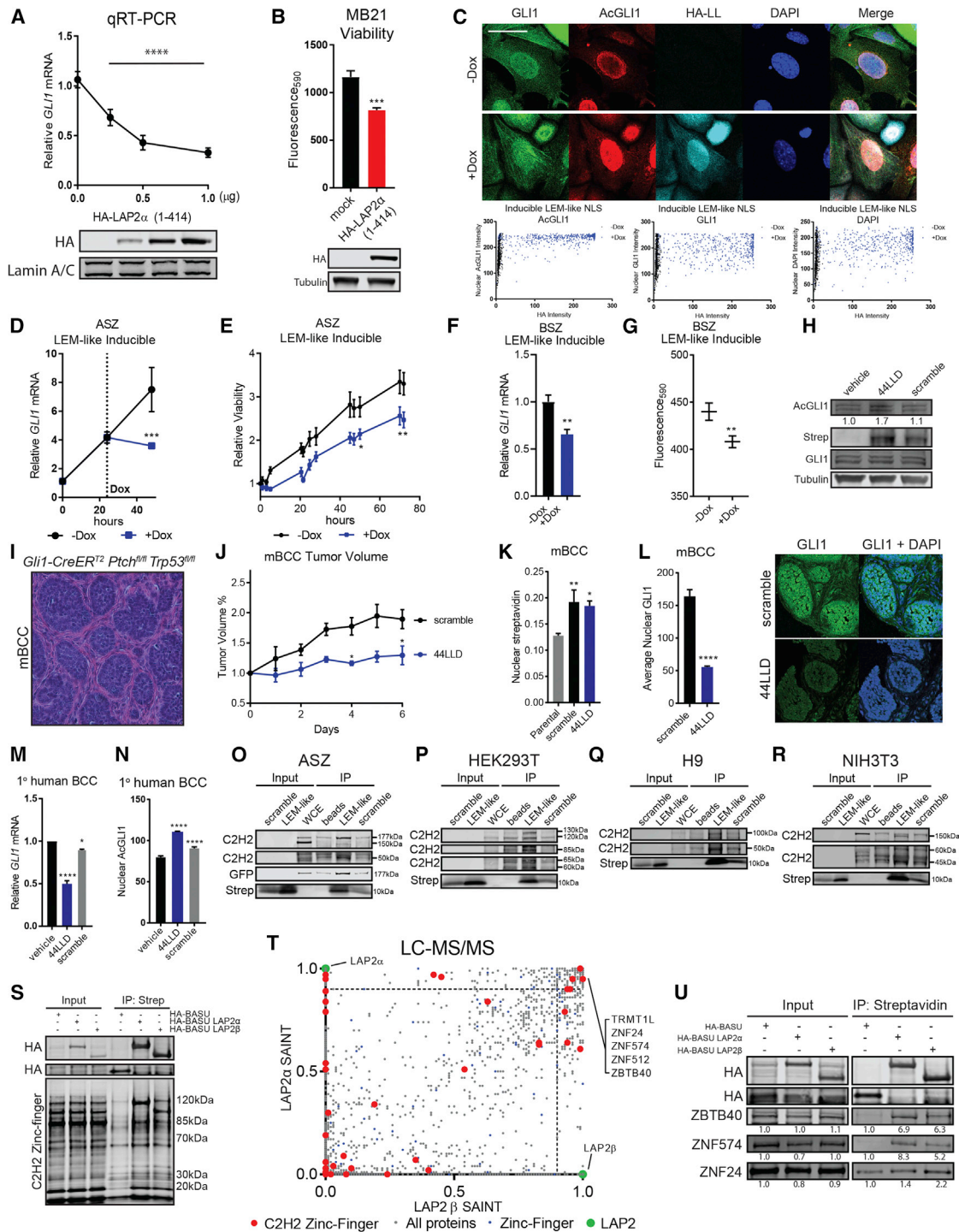
Figure 6. Disruption of the LAP2 Chaperoning System Inhibits GLI1 Activity

(A) qRT-PCR of *GLI1* normalized to *GAPDH* following transfection of LAP2α_{1-414} in ASZ cells (n = 9, ANOVA; x axis, micrograms of transfected DNA). An associated immunoblot is shown below.

(B) Cell viability measured by CellTiter Blue of MB21 cells electroporated with empty vector or LAP2α_{1-414} (n = 6, 2-tailed t test). An associated immunoblot is shown below.

(C) Immunofluorescence staining of the ASZ stable cell line with inducible expression of the HA-tagged LEM-like domain fused to a nuclear localization signal (NLS) (HA-LL; scale bar, = 20 μm). Shown is quantification of induction of HA-LL and the associated AcGLI1, GLI1, and DAPI (n = 1,232 nuclei).

(D) qRT-PCR of *GLI1* and *GAPDH* during induction of LEM-like domain NLS fusion (n = 9, 2-way ANOVA).

(legend continued on next page)

Cell

the presence of either LAP2α or HDAC1, and the reintroduction of exogenous *in-vitro*-translated LAP2α rescued HDAC1 binding to GLI1 (Figures 5E and S6F). To assess the effect of LAP2α: HDAC1 on GLI1 acetylation, a vorinostat pulse-chase experiment was performed in the context of LAP2α overexpression. In contrast to LAP2β overexpression (Figure 3N), LAP2α overexpression correlated with accelerated GLI1 deacetylation and a lower AcGLI1 to GLI1 resting ratio (Figures 5F and S6G). Immunofluorescence imaging of AcGLI1 during a vorinostat pulse-chase yielded central nuclear clearing of AcGLI1 over time, consistent with LAP2α acting on AcGLI1 in the nucleoplasm (Figure 5G). These data indicate that LAP2α physically interacts with HDAC1 and scaffolds a complex with GLI1.

The effect of LAP2α and HDAC1 on GLI1 nuclear export presents a conundrum because deacetylation should promote GLI1 nuclear export (Figure 2), whereas LAP2α's canonical anchorage to the nucleoskeleton should protect GLI1 nuclear positioning (Naetar et al., 2008). To address this, we interrogated the effect of LAP2α overexpression on CRM1 binding to GLI1. CoIP of GLI1 from HEK293T cells overexpressing increasing amounts of LAP2α demonstrated an inverse correlation between LAP2α and CRM1 binding to GLI1 (Figures 5H and S6H). In contrast, exogenous *in-vitro*-translated LAP2α failed to compete CRM1 off of GLI1 (Figure S6I). Together, this supports the idea that LAP2α antagonizes CRM1 binding to GLI1 in a cellular context. To interrogate how LAP2α exerts this effect, we performed coIP of GLI1 from HEK293T cells overexpressing LAP2α$_{1-414}$, a truncation that removes the lamin-binding domain (Naetar et al., 2008) but retains the GLI1-binding domain. Remarkably, disruption of the lamin-binding domain of LAP2α eliminated its ability to interfere with GLI1:CRM1 binding in cells (Figure 5H). Further, FRAP analysis of GFP-GLI1 in the context of LAP2α$_{1-414}$ demonstrated a larger nuclear mobile fraction compared with the control, approaching diffusion-limited GFP (Figures 5I, S3J, and S6J). Finally, coIP of a mutant GLI1 that disrupts LAP2α binding, GLI1$_{T296E}$, also failed to associate with lamin A (Figure 5J). These data indicate that LAP2α antagonizes

GLI1 nuclear export via its lamin binding; however, the mechanism by which this effect is exerted is not yet clear.

Next we investigated whether the LAP2α:GLI1 complex forms on DNA and chromatin. An electrophoretic mobility shift assay (EMSA) of GLI1 demonstrated supershifting of the GLI1:DNA complex upon addition of wheat germ cell extract *in-vitro*-translated LAP2α but not a BSA control (Figures 5K and S6K). As an additional control, we observed no LAP2α binding alone to the GLI binding site oligonucleotide, indicating that the LAP2α LEM-like domain does not harbor intrinsic affinity for this site. Furthermore, we observed no increase in GLI1 affinity for DNA with LAP2α addition, arguing that LAP2α tethers but does not alter GLI1 binding to DNA (Figure S6K). Finally, we sought to determine the genomic localization of both LAP2α and GLI1, utilizing DamID. If GLI1 and LAP2α co-occupy sites on chromatin, then GLI1-Dam and LAP2α-Dam fusion proteins should methylate similar DNA sequences. Indeed, qPCR of DamID-labeled chromatin from GLI1-Dam or LAP2α-Dam-expressing cells demonstrated enrichment at canonical GLI1 loci compared with a Dam-only control but not at non-GLI binding loci (Figures 5L, S6L, and S6M). Together, these data indicate that LAP2α forms an activating complex with deacetylated GLI1 on chromatin.

Disruption of the LAP2 Chaperoning System Inhibits GLI1 Activity

To assay the functional significance of the LAP2 chaperoning system, we disrupted the association of GLI1 with LAP2 by introduction of competing LEM-like domains. Overexpression of LAP2α$_{1-414}$, which retains the ability to bind to GLI1 but disrupts many of the endogenous functions of LAP2α (Figures 5H and 5I; Bradley et al., 2007; Naetar et al., 2008), should act as a dominant negative by saturating LAP2 binding sites on GLI1. LAP2α$_{1-414}$ overexpression significantly reduced GLI1 transcriptional activity in BCC cells (Figure 6A). Consistent with loss of GLI1 activity, LAP2α$_{1-414}$ overexpression also caused loss of cell viability in Hh-dependent cells (Figure 6B). We sought to

(E) ASZ cell viability following LEM-like domain induction (n = 12, 2-way ANOVA).

(F) qRT-PCR of the *GLI1* transcript normalized to *GAPDH* in BSZ cells following 24-hr LEM-like domain induction (n = 9, 2-tailed t test).

(G) BSZ cell viability assayed by CellTiter-Blue after 24 hr of LEM-like domain induction (n = 12, 2-tailed t test).

(H) Immunoblot of streptavidin (Strep) and AcGLI1/GLI1 (quantified) from ASZ cells treated with biotinylated TAT-LEM-like domain (44LLD) or TAT-scramble.

(I) H&E-stained tumor section from a *Gli1-CreER^{T2}, Ptch$^{fl/fl}$, Trp53$^{fl/fl}$* mouse.

(J) Volume change of mBCC over the treatment time course (n = 4, 2-way ANOVA).

(K) Quantitation of nuclear streptavidin normalized to DAPI from immunofluorescence staining of tumors following treatment with biotinylated cell-penetrant peptides (n = 15 [parental], 11 [44LLD], and 12 [scramble] high-power fields; ANOVA).

(L) Confocal image and quantitation of nuclear GLI1 from immunofluorescence staining of tumors following treatment with peptides (n = 12 high-power fields, ANOVA).

(M and N) qRT-PCR of the *GLI1* transcript normalized to *GAPDH* of primary human BCCs treated *ex vivo* with 44LLD or scramble (M, n = 3, ANOVA), and quantitation of nuclear AcGLI1 immunostaining (N, n = 10 fields, ANOVA).

(O–R) CoIP of biotinylated LEM-domain, scramble, or unbound beads followed by WCE in ASZ (O), HEK293T (P), H0 9 (Q), or NIH3T3 (R) cells. Shown is an immunoblot with streptavidin, GFP (in ASZ cells), and pan-C2H2 zinc-finger (C2H2 ZF) antibodies. Molecular weights of C2H2 ZF bands enriched in LEM-like are indicated.

(S) Immunoblot from BASU labeling with the indicated LAP2 isoforms for HA and pan-C2H2 zinc finger. The molecular weights of C2H2 ZF enriched in LAP2α or LAP2β over BASU are indicated.

(T) LC-MS/MS of gel slices from the BASU-LAP2 labeling experiment. Proteins are ranked by SAINT score (BASU-LAP2 versus BASU) and coded for non-zinc finger (gray), zinc finger (blue), C2H2 zinc finger (red), or LAP2 (green). The dotted line indicates a SAINT score of 0.9. C2H2 zinc-finger proteins and LAP2 are emphasized with larger circles.

(U) Immunoblot of the BASU-LAP2 labeling experiment with the indicated antibodies. Quantitations are normalized to the BASU-only control.

Error bars represent SE. Error bars were omitted when smaller than the width of associated data point symbol. *p < 0.05, **p < 0.01, ***p < 0.001, ****p < 0.0001.

Cell

refine the LAP2 segment interacting with the GLI1 zinc-finger domain and designed a 44-amino acid peptide based on the LAP2 LEM-like domain nuclear magnetic resonance (NMR) structure (Cai et al., 2001). We initially generated a doxycycline-inducible BCC cell line that produced exogenous LEM-like domains fused to a nuclear localization signal. Induction of these interfering LEM-like domains caused hyperacetylation of GLI1 (Figure 6C), correlated with a 50% reduction in Hh pathway output (Figure 6D) and decreased BCC cell viability (Figure 6E). We tested this in an additional BCC cell line and observed similar results (Figures 6F and 6G). To deliver this interfering peptide *in vivo*, we fused it to a cell-penetrant TAT domain peptide (44LLD) (Xia et al., 2001). We confirmed cellular entry and the induction of GLI1 hyperacetylation by immunoblot of cultured cells treated with 44LLD compared with a scrambled control (Figure 6H). Treatment of an established murine genetic model of BCC (Eberl et al., 2018) (*Gli1-CreER^{T2}, Ptch^{fl/fl}, Trp53^{fl/fl}*; Figure 6I) resulted in decreased Hh target expression and tumor burden (Figures 6J–6L). Treatment of primary human BCCs *ex vivo* with 44LLD peptide resulted in a 50% reduction of Hh pathway output (Figure 6M) and GLI1 hyperacetylation (Figure 6N). We conclude that disruption of the LAP2 chaperoning system inhibits GLI1 transcriptional output in BCC.

LAP2 Proteins Interact Broadly with Zinc-Finger Proteins

Because LAP2 proteins use their LEM-like domain to interact with the zinc-finger domain of GLI1, we investigated the generalizability of this interaction. Leveraging a pan-C2H2 zinc-finger antibody that recognizes a highly conserved linker region shared among most C2H2 zinc-finger proteins (Addison et al., 2015), we assessed whether any zinc-finger proteins co-immunoprecipitate with the LEM-like domain. CoIP of biotinylated LEM-like domains from whole-cell extract of ASZ cells expressing GFP-GLI1 revealed at least 4 zinc-finger proteins that enriched on the LEM-like domain 2-fold over the beads-only and scramble control. As expected, the dominant band observed at 177 kDa corresponded with GFP-GLI1 (Figure 6O). To determine whether zinc-finger proteins outside of GLI1 participate in LEM-like domain interaction, we repeated the experiment in three disparate cell lines that lack GLI1. In each cell line, we observed an array of zinc-finger proteins that interacted robustly with the LEM-like domain (Figures 6P and 6R). This indicates that the LEM-like domain is capable of interacting with diverse zinc-finger proteins that may vary by cell type.

To further investigate these putative interactions, we generated inducible BASU, BASU-LAP2α, and BASU-LAP2β-HEK293T cell lines. Vicinal labeling revealed multiple zinc-finger proteins that interacted with both LAP2 isoforms more robustly than the BASU control (Figure 6S) and appeared to correspond with bands observed with the LEM-like domain coIP (Figure 6P). To identify these interactors, we performed high-coverage mass spectrometry on three gel regions that harbored C2H2 zinc fingers that interacted robustly with LAP2α or LAP2β (Figure 6T; Tables S2, S3, and S4). Liquid chromatography-tandem mass spectrometry (LC-MS/MS) yielded 30,000–40,000 spectra that mapped to forward peptides and 18,000–25,000 spectra that mapped uniquely per gel region, and we analyzed 3 equivalent

gel regions for each BASU construct. LAP2α- or LAP2β-associated spectra were compared with the BASU control independently for each region and scored via CRAPome to generate SAINT scores. BASU-LAP2α selectively labeled LAP2α, and BASU-LAP2β labeled LAP2β, reinforcing the distinct nature of the two LAP2-isoform complexes. Focusing on only the strongest hits, we identified five C2H2 zinc-finger proteins that enriched on both LAP2α and LAP2β with SAINT scores of 0.9 or more and more than 3 spectra: ZNF512, ZBTB40, ZNF574, TRMT1L, and ZNF24. We reassessed these interactions by immunoblot and observed labeling above BASU control for ZBTB40, ZNF574, and ZNF24 (Figure 6U). These data indicate that LAP2 proteins interact with diverse zinc-finger proteins, suggesting a general nuclear scaffolding function.

DISCUSSION

Recent human and murine genetic studies revealing the central role of the primary cilium in regulating GLI activation in the cytoplasm stand in stark contrast to the relatively poor understanding of nuclear GLI regulation. Guided by two BCC resistance mechanisms, epistatic to ciliary Hh inhibition (Mirza et al., 2017), our work identifies a nuclear chaperoning system that regulates GLI1 activation. In this study, we demonstrate how nuclear lamina and nucleoplasmic splice variants of LAP2 modulate GLI1 acetylation or deacetylation to promote nuclear accumulation and subsequent activation to maintain high-level Hh pathway output during tumorigenesis. Disruption of the LAP2 chaperoning system appears promising for inhibition of Hh signaling in drug-resistant BCCs.

Our study identifies a LAP2β-dependent INM-bound pool of inactive AcGLI1 that is positioned for subsequent activation. Highlighting the importance of this inactive pool, its ablation reduces pathway output, and its overexpression is observed in human tumors. Furthermore, the generation of additional INM binding sites for GLI1 allows more rapid transcriptional recovery following transient HDAC inhibition without perturbing deacetylation kinetics, suggesting that this INM complex facilitates a nuclear GLI1 activation pathway. Investigating the composition and function of the INM-AcGLI1 complex remains a major focus of future work.

We further identify a nucleoplasmic LAP2α complex that competes with LAP2β to stabilize GLI1 on chromatin. Differing from previous reports of transcription factors diffusing off of the nuclear lamina, our data support a model where LAP2α acts as a chaperone that scaffolds an interaction with HDAC1 and antagonizes LAP2β binding. The BCC tumor resistance kinase aPKC promotes Smoothened inhibitor resistance by driving the accumulation of the LAP2α:HDAC1:GLI1 activation complex. Understanding the sequence of the GLI1 activation complex on chromatin (Whitson et al., 2018) represents an exciting avenue for study.

A major surprise during our work was the identification of a key functional interaction between the GLI1's non-DNA-binding zinc fingers and the LAP2 LEM-like domain. Indeed, many zinc fingers, the most common fold in biology, appear to lack DNA-binding activity (Cassandri et al., 2017). We find putative interactions between the LEM-like domain of the LAP2 proteins and

Cell

diverse C2H2 zinc-finger proteins. Determining the generalizability of the LEM-like domain interaction to other zinc-finger transcription factors provides an exciting avenue for future investigation.

STAR★METHODS

Detailed methods are provided in the online version of this paper and include the following:

- KEY RESOURCES TABLE
- CONTACT FOR REAGENT AND RESOURCE SHARING
- EXPERIMENTAL MODEL AND SUBJECT DETAILS
    - Cell Culture
    - Primary Patient BCC Explants
    - Ptch^fl/fl Gli1-CreER^T2 Trp53^fl/fl mice
- METHOD DETAILS
    - Fractionation
    - Nuclear Envelope Lift Off Assay
    - Triton Extraction Assay
    - BASU Vicinal Labeling
    - APEX2 Vicinal Labeling
    - Immunoprecipitation
    - *In vitro* translation
    - Vorinostat Pulse-Chase
    - Fluoresence Recovery After Photobleaching (FRAP) and Live Cell Imaging
    - Immunofluorescence and Fluorescence Imaging
    - Proximity Ligation Assay
    - 3D Structure Illumination Microcopy
    - Acetyl-GLI1 Antibody Generation
    - Electrophoretic Mobility Shift Assay (EMSA)
    - DamID
    - Quantitative Reverse Transcription PCR
    - Immunobloting
    - Cloning and Vectors
    - Mass Spectrometry
    - siRNA
- QUANTIFICATION AND STATISTICAL ANALYSIS

SUPPLEMENTAL INFORMATION

Supplemental Information includes six figures, four tables, and four videos and can be found with this article online at https://doi.org/10.1016/j.cell.2018.10.054.

AUTHOR CONTRIBUTIONS

A.N.M. and A.E.O. designed the experiments and wrote the manuscript. A.N.M. carried out the majority of the experiments. The majority of cellular or molecular experiments were assisted and optimized by N.M.U., S.A.M., and A.S.B. S.Z.A. and T.H. provided human tumor samples and annotation.

DECLARATION OF INTERESTS

The authors declare no competing interests.

REFERENCES

Addison, J.B., Koontz, C., Fugett, J.H., Creighton, C.J., Chen, D., Farrugia, M.K., Padon, R.R., Voronkova, M.A., Mclaughlin, S.L., Livengood, R.H., et al. (2015). KAP1 Promotes Proliferation and Metastatic Progression of Breast Cancer Cells. Cancer Res. 75, 344–355.

Atwood, S.X., Li, M., Lee, A., Tang, J.Y., and Oro, A.E. (2013). GLI activation by atypical protein kinase C ι/λ regulates the growth of basal cell carcinomas. Nature 494, 484–488.

Brachner, A., and Foisner, R. (2011). Evolvement of LEM proteins as chromatin tethers at the nuclear periphery. Biochem. Soc. Trans. 39, 1735–1741.

Brachner, A., and Foisner, R. (2014). Lamina-associated polypeptide (LAP)2α and other LEM proteins in cancer biology. Adv. Exp. Med. Biol. 773, 143–163.

Bradley, C.M., Jones, S., Huang, Y., Suzuki, Y., Kvaratskhelia, M., Hickman, A.B., Craigie, R., and Dyda, F. (2007). Structural basis for dimerization of LAP2alpha, a component of the nuclear lamina. Structure 15, 643–653.

Cai, M., Huang, Y., Ghirlando, R., Wilson, K.L., Craigie, R., and Clore, G.M. (2001). Solution structure of the constant region of nuclear envelope protein LAP2 reveals two LEM-domain structures: one binds BAF and the other binds DNA. EMBO J. 20, 4399–4407.

Canettieri, G., Di Marcotullio, L., Greco, A., Coni, S., Antonucci, L., Infante, P., Pietrosanti, L., De Smaele, E., Ferretti, E., Miele, E., et al. (2010). Histone deacetylase and Cullin3-REN(KCTD11) ubiquitin ligase interplay regulates Hedgehog signalling through Gli acetylation. Nat. Cell Biol. 12, 132–142.

Cassandri, M., Smirnov, A., Novelli, F., Pitolli, C., Agostini, M., Malewicz, M., Melino, G., and Raschellà, G. (2017). Zinc-finger proteins in health and disease. Cell Death Discov. 3, 17071.

Chow, K.-H., Factor, R.E., and Ullman, K.S. (2012). The nuclear envelope environment and its cancer connections. Nat. Rev. Cancer 12, 196–209.

Coni, S., Antonucci, L., D'Amico, D., Di Magno, L., Infante, P., De Smaele, E., Giannini, G., Di Marcotullio, L., Screpanti, I., Gulino, A., and Canettieri, G. (2013). Gli2 acetylation at lysine 757 regulates hedgehog-dependent transcriptional output by preventing its promoter occupancy. PLoS ONE 8, e65718.

Eberl, M., Mangelberger, D., Swanson, J.B., Verhaegen, M.E., Harms, P.W., Frohm, M.L., Dlugosz, A.A., and Wong, S.Y. (2018). Tumor Architecture and Notch Signaling Modulate Drug Response in Basal Cell Carcinoma. Cancer Cell 33, 229–243.e4.

Gotic, I., and Foisner, R. (2010). Multiple novel functions of lamina associated polypeptide 2α in striated muscle. Nucleus 1, 397–401.

Guilluy, C., Osborne, L.D., Van Landeghem, L., Sharek, L., Superfine, R., Garcia-Mata, R., and Burridge, K. (2014). Isolated nuclei adapt to force and reveal a mechanotransduction pathway in the nucleus. Nat. Cell Biol. 16, 376–381.

Gulino, A., Di Marcotullio, L., Canettieri, G., De Smaele, E., and Screpanti, I. (2012). Hedgehog/Gli control by ubiquitination/acetylation interplay. Vitam. Horm. 88, 211–227.

Ho, C.Y., Jaalouk, D.E., Vartiainen, M.K., and Lammerding, J. (2013). Lamin A/C and emerin regulate MKL1-SRF activity by modulating actin dynamics. Nature 497, 507–511.

Hui, C.-C., and Angers, S. (2011). Gli proteins in development and disease. Annu. Rev. Cell Dev. Biol. 27, 513–537.

Cell

Kay, R.R., Fraser, D., and Johnston, I.R. (1972). A method for the rapid isolation of nuclear membranes from rat liver. Characterisation of the membrane preparation and its associated DNA polymerase. Eur. J. Biochem. 30, 145–154.

Kind, J., Pagie, L., de Vries, S.S., Nahidiazar, L., Dey, S.S., Bienko, M., Zhan, Y., Lajoie, B., de Graaf, C.A., Amendola, M., et al. (2015). Genome-wide maps of nuclear lamina interactions in single human cells. Cell 163, 134–147.

Kogerman, P., Grimm, T., Kogerman, L., Krause, D., Undén, A.B., Sandstedt, B., Toftgård, R., and Zaphiropoulos, P.G. (1999). Mammalian suppressor-of-fused modulates nuclear-cytoplasmic shuttling of Gli-1. Nat. Cell Biol. 1, 312–319.

Lam, S.S., Martell, J.D., Kamer, K.J., Deerinck, T.J., Ellisman, M.H., Mootha, V.K., and Ting, A.Y. (2015). Directed evolution of APEX2 for electron microscopy and proximity labeling. Nat. Methods 12, 51–54.

Lee, B., Lee, T.-H., and Shim, J. (2017). Emerin suppresses Notch signaling by restricting the Notch intracellular domain to the nuclear membrane. Biochim. Biophys. Acta Mol. Cell Res. 1864, 303–313.

Mirza, A.N., Fry, M.A., Urman, N.M., Atwood, S.X., Roffey, J., Ott, G.R., Chen, B., Lee, A.L., Brown, A.S., Aasi, S.Z., et al. (2017). Atypical Protein Kinase C - Histone Deacetylase 1 inhibitors cooperate in basal cell carcinoma treatment. J. Clin. Investig. Insight. 2, e97071.

Naetar, N., Korbei, B., Kozlov, S., Kerenyi, M.A., Dorner, D., Kral, R., Gotic, I., Fuchs, P., Cohen, T.V., Bittner, R., et al. (2008). Loss of nucleoplasmic LAP2alpha-lamin A complexes causes erythroid and epidermal progenitor hyperproliferation. Nat. Cell Biol. 10, 1341–1348.

Nili, E., Cojocaru, G.S., Kalma, Y., Ginsberg, D., Copeland, N.G., Gilbert, D.J., Jenkins, N.A., Berger, R., Shaklai, S., Amariglio, N., et al. (2001). Nuclear membrane protein LAP2beta mediates transcriptional repression alone and together with its binding partner GCL (germ-cell-less). J. Cell Sci. 114, 3297–3307.

Noubissi, F.K., Kim, T., Kawahara, T.N., Aughenbaugh, W.D., Berg, E., Longley, B.J., Athar, M., and Spiegelman, V.S. (2014). Role of CRD-BP in the growth of human basal cell carcinoma cells. J. Invest. Dermatol. 134, 1718–1724.

Oro, A.E., Higgins, K.M., Hu, Z., Bonifas, J.M., Epstein, E.H., and Scott, M.P. (1997). Basal cell carcinomas in mice overexpressing sonic hedgehog. Science 276, 817–821.

Pan, D., Estévez-Salmerón, L.D., Stroschein, S.L., Zhu, X., He, J., Zhou, S., and Luo, K. (2005). The integral inner nuclear membrane protein MAN1 physically interacts with the R-Smad proteins to repress signaling by the transforming growth factor-β superfamily of cytokines. J. Biol. Chem. 280, 15992–16001.

Poleshko, A., Shah, P.P., Gupta, M., Babu, A., Morley, M.P., Manderfield, L.J., Ifkovits, J.L., Calderon, D., Aghajanian, H., Sierra-Pagán, J.E., et al. (2017). Genome-Nuclear Lamina Interactions Regulate Cardiac Stem Cell Lineage Restriction. Cell 171, 573–587.e14.

Ramanathan, M., Majzoub, K., Rao, D.S., Neela, P.H., Zarnegar, B.J., Mondal, S., Roth, J.G., Gai, H., Kovalski, J.R., Siprashvili, Z., et al. (2018). RNA-protein interaction detection in living cells. Nat. Methods 15, 207–212.

So, P.-L., Langston, A.W., Daniallinia, N., Hebert, J.L., Fujimoto, M.A., Khaimskiy, Y., Aszterbaum, M., and Epstein, E.H., Jr. (2006). Long-term establishment, characterization and manipulation of cell lines from mouse basal cell carcinoma tumors. Exp. Dermatol. 15, 742–750.

Somech, R., Shaklai, S., Geller, O., Amariglio, N., Simon, A.J., Rechavi, G., and Gal-Yam, E.N. (2005). The nuclear-envelope protein and transcriptional repressor LAP2β interacts with HDAC3 at the nuclear periphery, and induces histone H4 deacetylation. J. Cell Sci. 118, 4017–4025.

Stevens, T.J., Lando, D., Basu, S., Atkinson, L.P., Cao, Y., Lee, S.F., Leeb, M., Wohlfahrt, K.J., Boucher, W., O'Shaughnessy-Kirwan, A., et al. (2017). 3D structures of individual mammalian genomes studied by single-cell Hi-C. Nature 544, 59–64.

Strom, A.R., Emelyanov, A.V., Mir, M., Fyodorov, D.V., Darzacq, X., and Karpen, G.H. (2017). Phase separation drives heterochromatin domain formation (Nat. Publ. Gr).

Whitson, R.J., Lee, A., Urman, N.M., Mirza, A., Yao, C.Y., Brown, A.S., Li, J.R., Shankar, G., Fry, M.A., Atwood, S.X., et al. (2018). Noncanonical hedgehog pathway activation through SRF-MKL1 promotes drug resistance in basal cell carcinomas. Nat. Med. 24, 271–281.

Xia, H., Mao, Q., and Davidson, B.L. (2001). The HIV Tat protein transduction domain improves the biodistribution of beta-glucuronidase expressed from recombinant viral vectors. Nat. Biotechnol. 19, 640–644.

Zastrow, M.S., Vlcek, S., and Wilson, K.L. (2004). Proteins that bind A-type lamins: integrating isolated clues. J. Cell Sci. 117, 979–987.

Zhao, X., Ponomaryov, T., Ornell, K.J., Zhou, P., Dabral, S.K., Pak, E., Li, W., Atwood, S.X., Whitson, R.J., Chang, A.L.S., et al. (2015). RAS/MAPK Activation Drives Resistance to Smo Inhibition, Metastasis, and Tumor Evolution in Shh Pathway–Dependent Tumors. Cancer Res. 75, 3623–3635.

Cell

STAR★METHODS

KEY RESOURCES TABLE

REAGENT or RESOURCE	SOURCE	IDENTIFIER
Antibodies		
AcGLI1	This paper	N/A
GLI1 (V812)	Cell signaling	Cat # 2534
GLI1	R&D Systems	Cat # AF3455
CRM1	Santa Cruz	Cat # sc-74454
pan-LAP2	Abcam	Cat # ab185718
LAP2α	Abcam	Cat # ab5162
LAP2β	BD Biosciences	Cat # 611000
Emerin	Abcam	Cat # ab156871
Man1	Abcam	Cat # ab124148
LEMD1	Origene	Cat # TA320077
Sun1	Abcam	Cat # ab103021
Sun2	Abcam	Cat # ab124916
Lamin B1	Abcam	Cat # ab90169
Lamin A+C	Abcam	Cat # ab8984
BANF1	Abcam	Cat # ab88464
Acetyl-lysine	Cell Signaling	Cat # 9441S
SuFu	Abcam	Cat # ab28083
Tubulin	DSHB	Cat # E7-c
Biotin (streptavidin)	Li-Cor	Cat # 926-32230
HDAC1	Santa Cruz	Cat # sc-7872
HDAC3	Cell Signaling	Cat # 3949S
FLAG-tag	Sigma	Cat # F1804
HA-tag	Abcam	Cat # ab9134
Myc-tag	Abcam	Cat # ab9132
GAPDH	Santa Cruz	Cat # sc-32233
HNF1	Santa Cruz	Cat # sc-135939
C2H2 Zinc-finger	Millipore	Cat # ABE1941
Bacterial and Virus Strains		
Stellar Competent Cells	Takara	Cat # 636766
Biological Samples		
Patient BCC Mohs Biopsies	Stanford Dermatology	N/A
Chemicals, Peptides, and Recombinant Proteins		
Recombinant Human CRM1 protein	Abcam	Cat # ab125980
Recombinant Human LAP2 protein	Abcam	Cat # ab151936
Biotin-LEM-like domain peptide	ElimBio	custom synthesis
Biotin-scramble peptide	ElimBio	custom synthesis
44LLD	Genescript	custom synthesis
Vorinostat	Selleckchem	Cat # S1047
Entinostat	Selleckchem	Cat # S1053
CRT0329868	(Mirza et al., 2017)	N/A
PSI (ZIP)	Tocris	Cat # 2549
Fugene 6	Promega	Cat # E2692
Lipofectamine RNAiMAX Transfection Reagent	ThermoFisher	Cat # 13778075

(Continued on next page)

Cell

Continued

REAGENT or RESOURCE	SOURCE	IDENTIFIER
Critical Commercial Assays		
RealTime-Glo MT Cell Viability Assay	Promega	Cat # G9711
CellTiter-Blue Cell Viability Assay	Promega	Cat # G8080
Duolink *In Situ* Red Starter Kit	Sigma	Cat # DUO92101
Rabbit Reticulocyte *In vitro* translation kit	Promega	Cat # L2080
Wheat Germ *In vitro* translation kit	Promega	Cat # L4130
Deposited Data		
Mass Spectrometry BASU-labeling	This paper	Tables S2, S3, and S4
Experimental Models: Cell Lines		
MOUSE: MB21	Zhao et al., 2015	NA
Mouse: ASZ001	(So et al., 2006)	N/A
Mouse: BSZ	(So et al., 2006)	N/A
Human: UW-BCC	(Noubissi et al., 2014)	N/A
Mouse: NIH 3T3	ATCC	Cat # CRL-1658
Human: HEK293T	ATCC	Cat # CRL-3216
Experimental Models: Organisms/Strains		
Ptch$^{fl/fl}$, Gli1-CreERT2, Trp53$^{fl/fl}$	(Eberl et al., 2018)	N/A
NOD.Cg-Prkdc^{scid} Il2rgtm1Wjl/SzJ	Jackson Lab	Cat # 005557
Oligonucleotides		
Emerin siRNA 1	Sigma	SASI_Mm01_00089246
Emerin siRNA 2	Sigma	SASI_Mm01_00089247
Emerin siRNA 3	Sigma	SASI_Mm01_00089248
Man1 siRNA 1	Sigma	SASI_Mm02_00296101
Man1 siRNA 2	Sigma	SASI_Mm02_00296102
Man1 siRNA 3	Sigma	SASI_Mm02_00296103
LAP2α siRNA 1	Sigma	SASI_Mm02_00293323
LAP2α siRNA 2	Sigma	SASI_Mm02_00293324
LAP2α siRNA 3	Sigma	SASI_Mm02_00293325
LAP2β siRNA 1 CAGAGGAGCGAAGAGUAGAdTdT	Sigma	custom synthesis
LAP2β siRNA 2 GCAUGCAUCUUCUAUUCUGdTdT	Sigma	custom synthesis
LAP2β siRNA 3 UGGACGAGUGGAUCUUCAAdTdT	Sigma	custom synthesis
sgRNA LAP2β	Table S1	N/A
EMSA GLI1 Oligo ACGTGGACCACCCAAGACGAA	Genescript	N/A
DamID qPCR primers	see DamID methods	N/A
GLI1 (FAM-MGB probe Mm00494654_m1)	Life Technologies	Cat. # 4351370
GAPDH (Mm99999915_g1)	Life Technologies	Cat # 4352339E
Hprt (Mm01545399_m1)	Life Technologies	Cat # 4448485
Recombinant DNA		
pCS2FLAG	Addgene	Plasmid #16331
pCS2HA	Addgene	Plasmid #16330
pLex	Addgene	Plasmid #41390
APEX2	Addgene	Plasmid #79056
BASU	Addgene	Plasmid #107250
DamID	Addgene	Plasmid #59201
HDAC1	Addgene	Plasmid #13820
LAP2β	Addgene	Plasmid #21047
LAP2α	Genecopia synthesis	N/A

Cell

CONTACT FOR REAGENT AND RESOURCE SHARING

Further information and requests for resources and reagents should be directed to and will be fulfilled by the Lead Contact, Anthony Oro (oro@stanford.edu).

EXPERIMENTAL MODEL AND SUBJECT DETAILS

Cell Culture

MB21 cells (gender: male) were grown in DMEM:F12 (Thermo Fisher) supplemented with B27 (Thermo Fisher). ASZ001 (ASZ, gender: female) BCC cells were cultured in 154CF media (Life Technologies) supplemented with 2% chelated fetal bovine serum, Human Kerytinocyte Growth Supplement (Thermo Fisher), Penn-strep, and 0.05mM CaCl2. Experiments assaying Hh signaling carried out in serum-free conditions.

NIH 3T3 (gender: male) and HEK293T (gender: female) cells were cultured in DMEM supplemented with 10% fetal bovine serum (FBS). Experiments assaying Hh signaling were carried out in 0%–0.2% FBS supplemented with Smoothened Agonist (SAG, Sigma).

Mammalian cell transfection performed using FuGENE 6 Transfection Reagent (Promega), Lipofectamine LTX with Plus Reagent (Thermo Fisher), and MEF 1 Nucleofector Kit (Lonza) per manufacturer protocol. Transient transfection mammalian expression vectors are included below. Stable expression produced by piggybac transposition.

Primary Patient BCC Explants

This study was approved by the Stanford University Institutional Review Board #18325, with a waiver of consent from participants. Since the samples are de-identified for privacy reasons, gender identity of the specimens cannot be reported. Central biopsies of clinically diagnosed BCC tumor specimens from Mohs Surgery patients at the Stanford Dermatology Clinic were quatered and cultured in EpiLife Media (Life Technologies) +CaCl$_2$ with or without 20μM vorinostat for 3 hours. Specimen were flash frozen in OCT freezing media for subseqent assays.

Ptch$^{fl/fl}$ Gli1-CreER^{T2} Trp53$^{fl/fl}$ mice

All mice were housed under standard conditions, and animal care was in compliance with the protocols approved by the Institutional Animal Care and Use Committee (IACUC) at Stanford University. *Ptch$^{fl/fl}$, Gli1-CreER^{T2}, Trp53$^{fl/fl}$* mice were generated and used to generate BCC tumors as described previously (Eberl et al., 2018). For these studies we used only female mice due to the ability to house multiple per cage. Female mice aged 7.5 weeks were induced with 0.25mg of 4-hydroxytamoxifen per day for three consecutive days and exposed to 4 GY irradiation using an X-Ray irradiator on the fourth day. After an average of 3-5 months post-irradiation, tumors were passaged into NOD SCID gamma mice. 44LLD or scramble (50μg) was administered to passaged tumors by intra-tumoral injection once daily for eight consecutive days. Tumor volumes were measured by calipers, and Hh pathway output was asssesed by immunostaining for GLI1.

METHOD DETAILS

Fractionation

To prepare nuclear extracts, cells were resuspended in hypotonic lysis buffer (10mM HEPES pH7.9, 1.5mM MgCl2, and 10mM KCl) and dounce homogenized. Isolated nuclei were pelleted and resuspended in RIPA buffer. Proteasome inhibitor (MG132, 10μM) was added to observe GLI1 export due to the short half-life of GLI1 in the cytoplasm.

The protocol for nuclear envelope fractionation was adapted from previous reports(Kay et al., 1972). Isolated nuclei were resuspended in Nuclear Envelope Buffer 1 (10mM Tris 8.5, 0.MgCl2, 5mM β-ME, 10% sucrose, DNase I) and incubated at room temperature for 10 minutes to lyse the nuclear membrane and gently remove the nucleoplasmic fraction, characterized by the initial release of lamin A. The crude nuclear envelope, containing non-intergral membrane bound INM components, was pelleted at 38k r*cf.*, resuspended in Nuclear Envelope Buffer 2 (10mM Tris 7.4, 0.MgCl2, 5mM β-ME, 10% sucrose, DNase I), and allowed to incubate at room temperature for 15 minutes. This allowed for the release of peripheral chromatin and non-intergral membrane INM proteins, characterized by the release of BANF1. Purified nuclear envelopes were resuspended in RIPA to solubilize the remaining peptides.

Nuclear Envelope Lift Off Assay

ASZ cells were serum starved for 24hrs to induce the Hh pathway, then treated with 20μM vorinostat to hyperacetylate GLI1 and drive it onto the nuclear envelope. Crude nuclear envelopes were isolated (see Nuclear Envelope Fractionation protocol above; crude nuclear envelopes correspond to pelleted sample after Nuclear Envelope Buffer 1 lysis) and resuspended in PBS (supplemented with 0.5mM DTT, 5 μM ZnCl2, 5 mM MgCl2 and 1 mM NAD+) or PBS + recombinant CobB deacetylase (a generous gift from the lab of Dr. Peter Jackson) (supplemented with 0.5mM DTT, 5 μM ZnCl2, 5 mM MgCl2 and 1 mM NAD+). CobB is a *E. coli* derived non-specific deacetylase. The deacetylation reaction was allowed to proceed for 30mins. Nuclear envelopes were pelleted by centrifugation (15k rpm). Supernatant, containing protiens release following deacetylation, was collected in Laemmli sample buffer corresponding to the ''Lift off'' sample. The pelleted nuclear envelopes were resuspended in RIPA, corresponding to the ''output'' sample.

Cell

Triton Extraction Assay

ASZ cells were washed with PBS prior to incubation in 1% Triton X-100 in PBS supplemented with protease inhibitor cocktail for 10 minutes. Supernatant was collected and analyzed by dot blot with three technical replicates per experiment. Each condition was assayed independently three times as well.

BASU Vicinal Labeling

BASU fusions were stably expressed via piggybac transposition. 50μM d-biotin supplemented media was added to cells for 5 hours to allow labeling of proximal interactors. Cells were collected in RIPA lysis buffer supplemented with protease inhibitor and Pierce Universal Nuclease. Whole cell extract was homogenized by sonication and clarified by centrifugation. Free biotin was removed by iterative spin concentrate-dilution steps using spin concentration units (Millipore, MWCO:3kDa) to lower free biotin concentration by 125 fold. Purified lysate bound-biotin was quantied by dot blot and input bound-biotin was normalized prior to streptavidin pull-down (Dynabeads MyOne Streptavidin C1). Following stringent washing (3X 10mins RIPA, 2X 5min 2%SDS in PBS, 1X 1min RIPA), biotinylated proteins were eluted by boiling (95°C, 800rpm) in Laemmli sample buffer supplemented with 10mM biotin.

APEX2 Vicinal Labeling

An APEX2-GLI1 fusion was stably expressed in ASZ by lentiviral transduction. APEX labeling was performed as previously described (Lam et al., 2015). Briefly, biotin-phenol supplemented media was introduced 30 minutes prior to labeling. H_2O_2 was added to induce labeling and was quenched following 1 minute of labeling. Biotinylated species were purified as described above for BASU and immunoblotted.

Immunoprecipitation

All immunoprecipitation were in the absence of crosslinking. For the majority of experiments cell lysates were prepared in 1% Triton X-100 in TBS supplemented with protease and phosphatase inhibitors (Roche). Immunoblot of whole cell extract under these conditions confirmed solubilization of INM proteins. Anti-FLAG M2 Sepharose Beads (Sigma) and Pierce Anti-HA Magnetic Beads (Thermo Fisher) were pre-blocked in 5% BSA prior to incubation overnight. Washes were carried out at room temperature using lysis buffer (3X 3mins). Samples were eluted by boiling in Laemmli sample buffer.

For graded high salt washes, large scale co-IP experiments were carried out and subsequently aliquoted and washed seperately. For *in vitro* translated protein IP's, the indicated components were mixed and allowed to bind at 4°C for 1 hour prior to the addition of beads. Whole cell extracts for these experiments were generated by the lysis of HEK293T pellets in 1% Triton X-100 in TBS supplemneted with protease inhibitor. For experiments comparing LAP2 isoforms, the pan-LAP2 antibody was used thereby reducing error associated with different antibodies.

In vitro translation

Proteins of interest were generated *in vitro* using Promega's TnT Quick Coupled Rabbit Reticulocyte or Wheat Germ Cell Lysate Transcription/Translation System according to manufacturer's protocol. For *in vitro* translation, pCS2 vectors harboring SP6 promoters were utilized. In general, all *in vitro* translations utilized the rabbit reticulocyte lysate system. Where specifically indicated, wheat germ cell lysate was used to test for "direct" binding in a context without endogenous mammalian cofactors.

Vorinostat Pulse-Chase

ASZ cells were serum starved for 24hrs and vorinostat (20μM) treated for 1hr. Vorinostat media was replaced with fresh prewarmed media to allow deacetylation to take place. Cells were collected in RIPA buffer supplemented with protease inhibitor and 1mM Sodium Butyrate to hault deacetyation. Cell extracts were spotted onto nitrocellulose and immunoblotted. Each time point represents three biological replicates with three technical replicates each.

Fluoresence Recovery After Photobleaching (FRAP) and Live Cell Imaging

Live cell imaging and FRAP experiments were carried out in cells plated onto Nunc Lab-Tek Chambered Coverglass coated with poly-D lysine. Prior to imaging, cells were placed in Flourobright media supplemented with Hoescht HCl. Live floresence imaging on Leica SP8 White Light Confocal (100x objective) equiped with Hybrid detectors housed in a temperature, humidity, and CO_2 regulated imaging chamber. Bleaching area (5 μm in diameter) were constant and bleaching intensity was determined empirically to produce even bleach points. Recovery was observed in 2 s intervals using Leica LAX software and analyzed in Prism.

Immunofluorescence and Fluorescence Imaging

Cells were fixed in 4% formaldehyde in phosphate buffered saline and prepared per a general immunofluorescence protocol (abcam). Primary antibodies were used at the manufacturers' recommended concentration. Fluorescent-labeled secondary antibodies utilized: Alexa Fluor 488, Alexa Fluor 555, Alexa Fluor 594, and Alexa Fluor 647 (1:500, Life Technologies). Confocal imaging was carried out using a Leica SP8 microscope equipped with adjustable white light laser and hybrid detectors.

Images were quantified using ImageJ or ICY image analysis software, and when making comparisons between images laser intensities and imaging settings were held constant. Occasionally an imaging control, such as LAP2β, whose expression is

Cell

independent of the experimental variable was utilized to normalize for staining variability across a specimen. To draw scale bars, Lieca LAX software was used.

Radial GLI1/AcGLI1 distributions were calculated by line averaging on unique nuclei with the line starting in the nucleoplasm, ending in the cytoplasm, and centering on the edge of the DAPI signal. The 90% reduction point of the DAPI signal was indicated as the nuclear envelope and marked with a dotted line. Standard error is displayed as thin dotted radial tracings.

Proximity Ligation Assay

Proximity Ligation Assays were conducted per manufacturer's protocol (Duolink/ Sigma) to detect interaction between endogenous proteins in a cellular context. Notably, PLA experiments all involve the change in signal between an antibody pairs under experimental perturbation. In our experience, it is inappropriate to compare different antibody pairs and single antibody controls inadequately assess specificy. PLA signal was measured using constant imaging setting and averaged across fields. Puncta were quantified for cell line PLA experiments while total PLA floresence signal was quantified for tissues due to the lack of clear puncta separation.

3D Structure Illumination Microcopy

ASZ cells were cultured on poly-D lysine coated high performance 0.17mm coverglass (Zeiss). OMX BLAZE 3D-Structured Illumination Super Resolution Microscope (Stanford University Cell Sciences Imaging Facility). System specifications: OMX V4 microscope platform with X, Y, Z Nanomotion stage movers with 25 mm travel; OMX BLAZE SI patterns generated using an electro-optical high-speed SI diffraction grating engine; Piezo controlled Fast Z axis system - 100 micron range; 60X, N.A. 1.30silicon immersion objective for matching of refractive indexes during live cell imaging; Offline workstation with SoftWoRx software for generating SI image reconstructions.

Acetyl-GLI1 Antibody Generation

Antibodies and peptides were generated by 21st Century Biochemicals. Animals were injected with both human (Acetyl-IGTRGL [K-ac]LPPLPHT-Ahx-C-amide) and mouse (Acetyl-IGSRGL[K-ac]LPSLTHA-Ahx-C-amide) HPLC-purified immunogenic Acetyl-K518 GLI1 peptides. Affinity purified antibodies were generated by the column purification.

Electrophoretic Mobility Shift Assay (EMSA)

Recombinant zinc-finger GLI1-GST fusion protein and wheat germ cell *in vitro* translated LAP2α was incubated with a LICOR IR-dye labeled oligonucleotide harboring GLI1 binding motif (Genescript, ACGTGGACCACCCAAGACGAA) were run on a 6% DNA Retardation Gel (ThermoFischer), and imaged using Odyssey CLx (Li-Cor). Mock lane is empty GST vector transfected bacterial lysate. We note that LAP2α did not induce a clean supershifted band, but a supershifted smear. This is indicative of a micromolar interaction which would struggle to remain stable during an EMSA which requires interactions in the nanomolar range.

DamID

The DamID technique was performed following the original protocol discussed well in the van Steensel lab website (http://research. nki.nl/vansteensellab/DamID.htm). Briefly, GLI1 and LAP2α were inserted amino-terminal to DamID in an inducible vector obtained from the van steen lab (via Addgene), or carboxy-terminal to LAP2β in a piggybac transposition vector. Stable lines were generated by stable chemostransfection (Lipofectamine LTX) of linearized vectors in NIH 3T3 cells and geneticin selected as recommended, or by piggybac transposition followed by hygromycin selection. Integration was determined by PCR of genomic DNA. Cells were serum starved and Smoothened Agonist (SAG) treated to activate Hh signaling. Genomic DNA was isolated and subjected to DpnI digestion which cuts DNA at the Damid-specific methylation of GATC motifs. Bioanalyzer tracings confirm that DamID is labeling and the spacing between the cut GATC motif produces the expected 200-500bp fragment peak. DamID adaptors were ligated followed by DpnII digestion to eliminate innapropriately ligated fragments. Next a methyl-PCR was performed to amplify DamID labeled DNA, followed by purification and analysis by qPCR. qPCR Primers:

Step-Target	Forward	Reverse
2-ptch1	acagggtggtggatagtgcg	tacgaggcgttgttccctgc
2-GLI1	cgccggcttcctaagggtta	Cggacagacgtctccgactc
3-nkx2-9	CTACCAAGCGTGCCTAAAGT	TTTATCCCAGGGAGCTAAAG
3-ACTB	GGCACCACACCTTCTACAAT	GTTACCCGGGATACTGACCT
3-JUNB	CAGGAAGGCTGCAGTTACTCT	AGCGGCTTTCAACAGACC
3-NEUROG2	TTAACTGGAGTGCCTTGG	CTCGTGTGTTGTCGTTC
3-SMAD7	TTTTAAAGCGACAGGGTGTCTAGA	TCT GCT CGG CTG GTT CCA

Quantitative Reverse Transcription PCR

RNA isolated using QIAGEN RNeasy Mini Kit according to manufacturer protocol. TaqMan RNA-to-CT 1-Step Kit used for reverse transcription and quantitative PCR. TaqMan Gene Expression Assay Probes Life Technologies: GLI1 (FAM-MGB probe Mm00494654_m1); GAPDH (Mm99999915_g1); Hprt (Mm01545399_m1) used in an assay dependent concentration.

Immunobloting

Whole cell extracts were harvested using radioimmunoprecipitation (RIPA) buffer supplemented with protease and phosphatase inhibitors (Roche) and run on gradient SDS-PAGE gels (Life Technologies) followed by wet transferred onto nitrocellulose membranes (0.45microns, BioRad). Primary antibodies used in an assay dependent concentration in 5% Bovine Serum Albumin in TBST. Fluorescent secondary antibodies compatible with Odyssey CLx (Li-Cor) used for 2-color imaging of membranes.

Cloning and Vectors

pCS2FLAG (Addgene Plasmid #16331) and pCS2HA (Addgene Plasmid #16330) used to express epitope tagged protein in *in vitro* translation and mammalian cell culture. pGex and pQE-80L used to generate recombinant peptides. Piggybac transposition entry vector pbCAG (modifed from Addgene Plasmid #40973) and lentiviral transfecer vector pLex (modified from Addgene Plasmid #41390) utilized to generate stable lines. pEGFP-N3 used to generate GFP fusions for mammalian expression. To generate vicinal labeling constructs the follow plasmid were used: BASU (a generous gift from Dr. Paul Khavari), APEX2 (Addgene Plasmid #79056), DamID (Addgene #59201).

GLI1 source cDNA was derived from our lab's previous projects on GLI1. HDAC1 (Addgene Plasmid #13820), p300 (Addgene Plasmid #23252), HDAC3 (Addgene Plasmid #13819), LAP2α (synthesized by Genecopia) and LAP2β (Addgene Plasmid #21047).

NEB Q5 PCR mix used per manufacturers protocol to generate PCR inserts with primers synthesized by Elim BioPharm (Hayward, CA). In-Fusion (Clontech) recombination based cloning performed according to manufacturers protocol.

Mass Spectrometry

Mass spectrometry was performed by the Stanford University Mass Spectrometry Core. Samples were run on a 4%–12% SDS-PAGE gel and resolved by Coomassie staining. Gel bands were excised out in a 1.5 mL Eppendorf tubes and then cut in 1x1 mm squares. The excised gel pieces were then reduced with 5 mM DTT, 50 mM ammonium bicarbonate at 55°C for 30 min. Residual solvent was removed and alkylation was performed using 10 mM acrylamide in 50 mM ammonium bicarbonate for 30 min at room temperature. The gel pieces were rinsed 2 times with 50% acetonitrile, 50 mM ammonium bicarbonate and placed in a speed vac for 5 min. Digestion was performed with Trypsin/LysC (Promega) in the presence of 0.02% protease max (Promega) in a standard overnight digest at 37°C. Samples were then centrifuged and the solvent including peptides were collected and further peptide extraction was performed by the addition of 60% acetonitrile, 39.9% water, 0.1% formic acid and incubation for 10-15 min. The peptide pools were dried in a speed vac. Samples were reconstituted in 12.5μl reconstitution buffer (2% acetonitrile with 0.1% Formic acid) and 3μl (100ng) of it was injected on the instrument.

Mass spectrometry experiments were performed using an Orbitrap Q-Exactive HFX mass spectrometer (Thermo Scientific, San Jose, CA) with liquid chromatography using a Nanoacquity UPLC (Waters Corporation, Milford, MA). For each LCMS experiment a flow rate of 250 nL/min was used, where mobile phase A was 0.2% formic acid in water and mobile phase B was 0.2% formic acid in acetonitrile. EASY-spray nanoLC analytical columns (Thermo Scientific) were used, measuring 50 cm in length and heated to 50 C. Peptides were directly injected onto the analytical column using a gradient (3%–45% B, followed by a high-B wash) of 80min. The mass spectrometer was operated in a data dependent fashion using HCD fragmentation for MS/MS spectra generation.

For data analysis, the .RAW data files were processed using Byonic v 2.14.27 (Protein Metrics, San Carlos, CA) to identify peptides and infer proteins. Proteolysis was assumed to be tryptic allowing for N-ragged cleavage with up to two missed cleavage sites. Precursor and fragment mass accuracies were held within 12 ppm. Proteins were held to a false discovery rate of 1%, using standard approaches.

siRNA

Sigma pre-designed siRNA were used for knockdown assays. Emerin: SASI_Mm01_00089246, SASI_Mm01_00089247, SASI_Mm01_00089248. Man1: SASI_Mm02_00296101, SASI_Mm02_00296102, SASI_Mm02_00296103. LAP2α: SASI_Mm02_00293323, SASI_Mm02_00293324, SASI_Mm02_00293325. LAP2β siRNA's were custom designed to avoid disrupting LAP2α.

QUANTIFICATION AND STATISTICAL ANALYSIS

Statistical test used in each experiment as well as information on replicates is indicated in the Figure Legends. In general three technical replicates were performed for each independent experiment. Significance values were generated using GraphPad PRISM 6 and denoted by asterisks as indicated in Figure Legends. Curve fitting for FRAP analysis and saturation binding was also performed in GraphPad PRISM 6. Western blot and EMSA quantitation were performed in LICOR Image Studio. Radial distribution was calculated using FIJI software. Scale bars were measured by Lieca LAS X software. Quantitation of immunofluorescence including automated nuclear quantitation and puncta counting were performed in ICY. Mass spectrometry data were computed first by Byonic v 2.14.27 and then CRAPome (please refer to specific section for further detail).
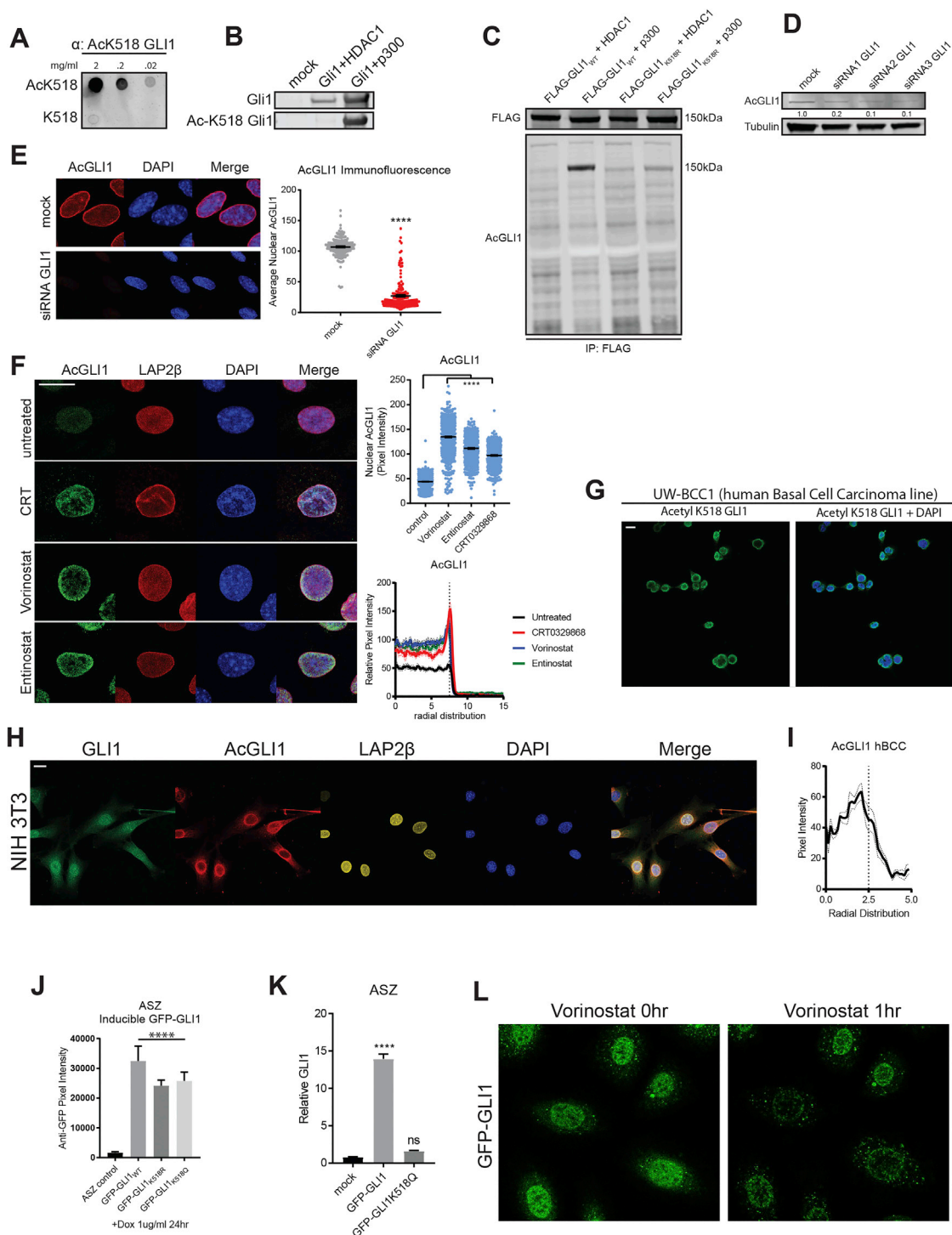
Figure S1. Related to Figure 1

(A) AcGLI1 antibody specificity tested by dot blot of AcGLI1 peptide versus deacetyl peptide corresponding the immunogen for antibody generation.

(B) Immunoblot with AcGLI1 antibody of FLAG-GLI1 co-transfected with p300 or HDAC1 in HEK293T.

(C) Uncropped immunoblot with AcGLI1 antibody on immunoprecipitation of indicated FLAG-GLI1 mutants co-transfected with acetylation modifiers.

(D) Immunoblot with AcGLI1 antibody on whole cell extract from ASZ transfected with indicated siRNA.

(E) Immunofluorescent staining with AcGLI1 antibody on ASZ transfected with indicated siRNA. Quantitation of nuclear AcGLI1 pixel intensity (n = 171 nuclei, 2-tailed t test).

(F) ASZ cells serum starved for 24 hours prior to treatment with pan-HDAC, vorinostat and entinostat, or aPKC$_\iota$, CRT0329868 (CRT), inhibitor. AcGLI1 nuclear pixel intensity quantified on top, (scale bar = 20μm; n = 706(control), 666(vorinostat), 427(entinostat), 422(CRT0329868); ANOVA), and radial distribution quantitated below (n = 42(untreated), 27(CRT), 25(vorinostat), 25(entinostat).

(G-H) NIH 3T3 (hedgehog-responsive fibroblast) and UV-BCC1 (hedgehog-dependent epithelial) both demonstrate the same sub-nuclear distribution of AcGLI1 (scale bar = 17μm).

(I) Quantitation of radial distribution of AcGLI1 in primary human BCC associated with Figure 1E (n = 10).

(J) Quantification of dot blot of GFP in GFP-GLI1 inducible lines and control ASZ following doxycycline treatment (n = 9, ANOVA).

(K) qRT-PCR of *GLI1* transcript normalized to *GAPDH* following expression of indicated GFP-GLI1 mutants (n = 9, ANOVA).

(L) Live cell imaging of GFP-GLI1 in ASZ following 1hr of vorinostat treatment.

Error bars represent standard error, ns = not significant, **p < 0.01, ****p < 0.0001.
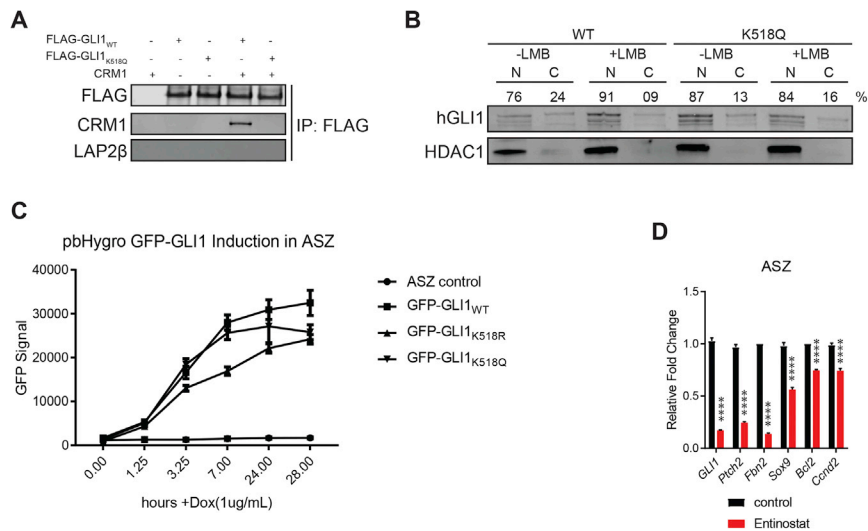
Figure S2. Related to Figure 2

(A) Co-IP of *in vitro* translated FLAG-GLI1 mutants with recombinant human CRM1 protein.

(B) Fractionation of NIH 3T3 transfected with GLI1$_{WT/K518Q}$ and treated with Leptomycin B (LMB, 10μM, 3hr).

(C) Quantification of dot blot of GFP in GFP-GLI1 inducible lines and control ASZ following doxycycline treatment over time course of 28hr (n = 9).

(D) qRT-PCR of indicated transcripts normalized to *HPRT1* from ASZ treated for 24 hour with HDAC inhibitor entinostat (n = 9, 2-tailed t test).

Error bars represent standard error, ****p < 0.0001.
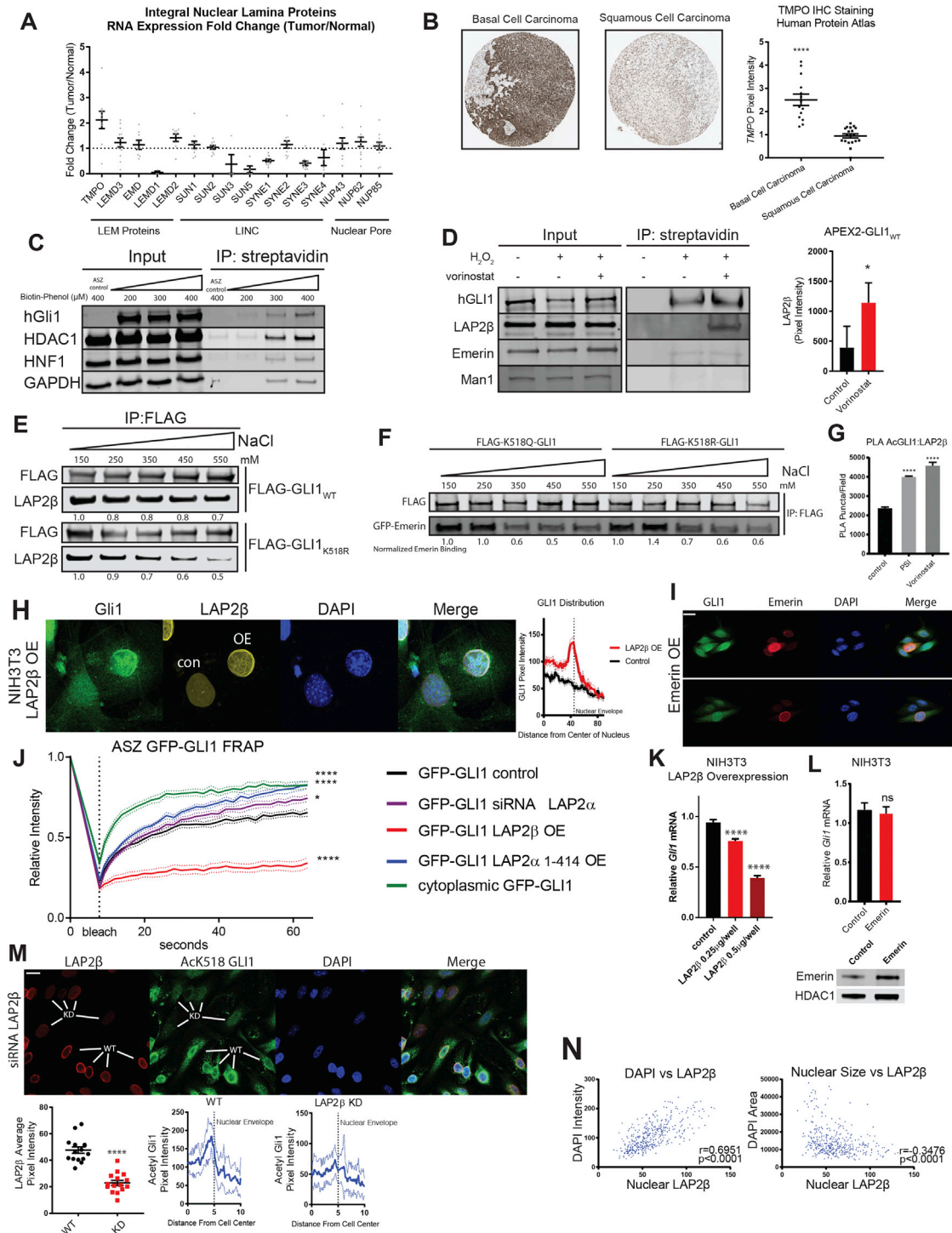
Figure S3. Related to Figure 3

(A) Fold change of FPKM values of indicates genes between matched tumor-normal pairs in primary human BCC by RNA sequencing (n = 12).

(B) Immunohistochemistry stain of LAP2 (TMPO) in BCC as well as squamous cell carcinoma from the Human Protein Atlas, with associated quantitation (n = 14(BCC), 19(SCC)).

(C) Optimization of APEX2-GLI1 ASZ stableline labeling efficiency as a function of biotin-phenol concentration. Immunoblot of human GLI1 (hGLI1, autolabeling of exogenous GLI1), HDAC1 (positive control), HNF1 (nuclear negative control), and GAPDH (cytoplasmic negative control).

(D) Streptavidin pulldown and immunoblot following vicinal labeling with APEX2-GLI1$_{WT}$ in ASZ ± H$_2$O$_2$ ± vorinostat (n = 5, 2-tailed t test).

(E) Co-IP of *in vitro* translated FLAG-GLI1$_{WT/K518R}$ following incubation in HEK293T whole cell extract washed over a gradient of high salt buffer.

(legend continued on next page)

(F) Co-IP of *in vitro translated* FLAG-GLI1$_{K518R/Q}$ with GFP-emerin washed with a gradient of high salt buffers.

(G) Quantitation of PLA puncta per field from experiment in Figure 3D (n = 10 fields, ANOVA).

(H) NIH 3T3 cells heterogeneously overexpressing (OE) LAP2β by transfection. Endogenous GLI1 redistribution after LAP2β OE quantified (n = 20, scale bar = 17μm).

(I) Immunofluorescence of Emerin OE demonstrates no effect on GLI1 distribution in ASZ (scale bar = 20μm).

(J) FRAP analysis of GFP-GLI1 in inducible ASZ line with the indicated perturbations (control: n = 10, $t_{1/2}$ = 8.9 s (7.5-10.7, 95%CI), mobile fraction = 64% (62.6-65.8, 95%CI); LAP2β OE: n = 9, $t_{1/2}$ = 9.3 s (4.6-24.7, 95%CI), mobile fraction = 32% (30.6-36.9, 95%CI); LAP2α$_{1-414}$ OE: n = 7, $t_{1/2}$ = 12.8 s (11.2-14.8, 95%CI), mobile fraction = 82% (80.2-85, 95%CI); siRNA LAP2α: n = 11, $t_{1/2}$ = 10.7 s (9.4-12.4, 95%CI), mobile fraction = 73% (71.5-75.4, 95%CI); cytoplasmic GFP-GLI1: n = 10, $t_{1/2}$ = 5.1 s (4.2-6.1, 95%CI), mobile fraction = 80% (79.6-82, 95%CI)).

(K) Transfection of LAP2β in NIH 3T3 produces a dose-dependent decrease in GLI1 transcriptional activity assayed by qRT-PCR of *GLI1* mRNA normalized to *GAPDH* (n = 9, ANOVA).

(L) Emerin transfection compared to empty vector control in NIH 3T3 followed by qRT-PCR (n = 9, 2-tailed t test) and associated immunoblot.

(M) siRNA knockdown (KD) of LAP2β in ASZ results in loss of AcGLI1 compared to wild-type (WT) by immunofluorescence(scale bar = 20μm, n = 15 cells, 2-tailed t test).

(N) Supporting Figure 3L, quantitation of nuclear size and DAPI intensity as a function of LAP2β depletion demonstrate an indirect and direct correlation, respectively. This supports previous reports. (n = 398 nuclei, Pierson correlation coefficients).

Error bars represent standard error, error bars omitted when smaller than the width of associated data point symbol, ns = not significant, *p < 0.05, **p < 0.01, ***p < 0.001, ****p < 0.0001.
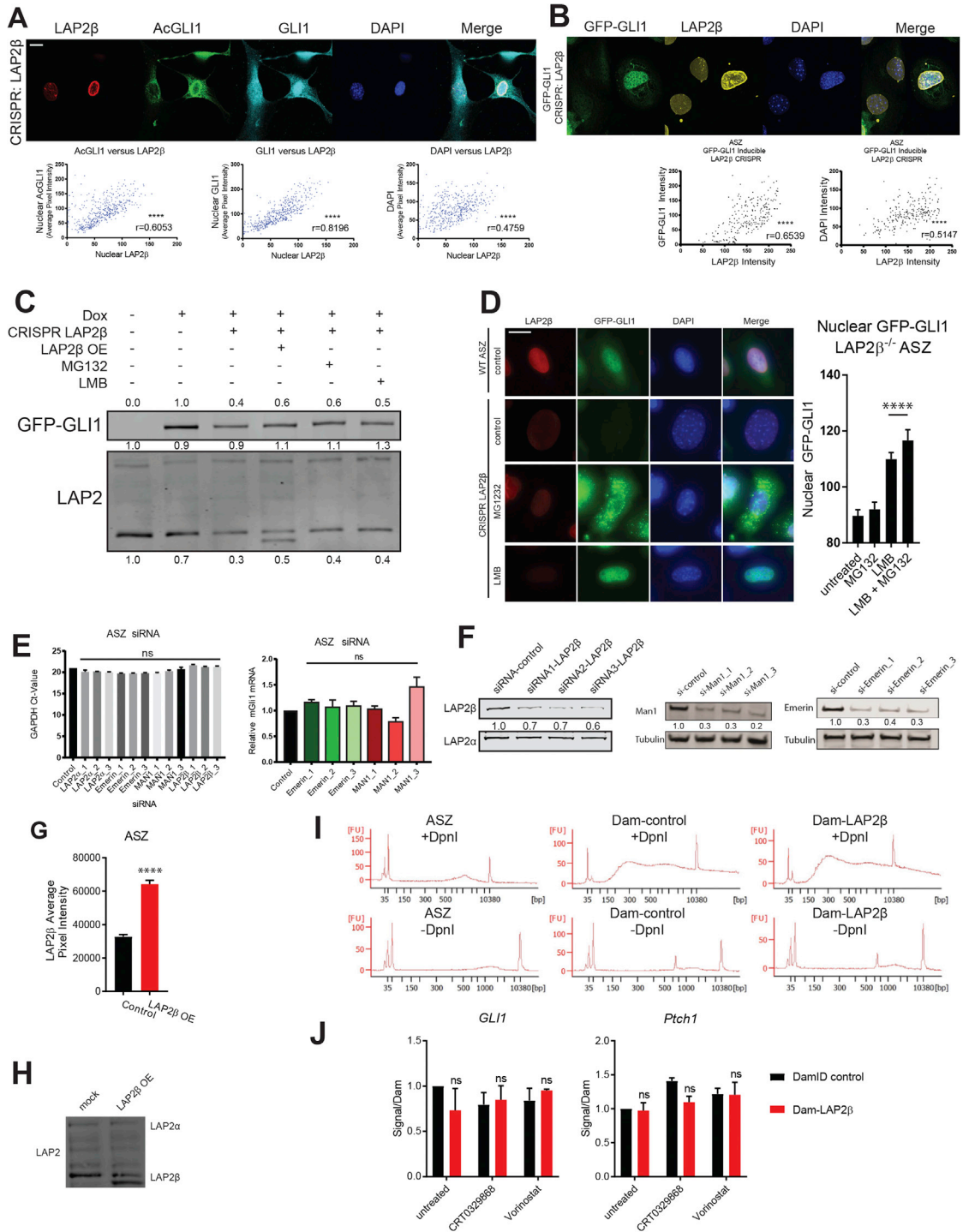
Figure S4. Related to Figure 3

(A) Cas9 and sgRNAs targeting the LAP2β-specific exon 6 of the TMPO gene were transiently expressed in NIH 3T3 generating a heterogeneously depleted population of cells. Total GLI1, and DAPI signal correlated with LAP2β knocked down (scale bar = 17μm, n = 488 nuclei, Pierson correlation coefficient). Please refer to Data Table S1 for details of guide-design.

(B) CRISPR-Cas9 depletion of LAP2β from GFP-GLI1 inducible ASZ stableline indicates loss of GLI1 stability. Nuclear GFP-GLI1 is lost upon LAP2β depletion (scale bar = 20 μm, n = 228 nuclei, Pierson correlation coefficient).

(C) Immunoblot of inducible GFP-GLI1 ASZ with LAP2β depletion by CRISPR followed by transfection with LAP2β (LAP2β OE) or treatment with MG132 or leptomycin B (2hr).

(legend continued on next page)

(D) Images and quantification of nuclear GFP-GLI1 in cells depleted of LAP2β following indicated drug treatments by immunostaining (n = 156(untreated), 126(MG132), 311(LMB), 147(MG132+LMB) nuclei, ANOVA). Scale bar = 20μm

(E) Ct-values from qRT-PCR of *GAPDH* following siRNA transfection indicates no changes to housekeeping gene expression (left, n = 9, ANOVA). Normalized *GLI1* transcript remains unaffected following emerin or MAN1a knockdown (right, n = 9, ANOVA).

(F) Immunoblots confirm knockdown of indicated siRNA targets supporting Figure 3M and S4E.

(G) Quantitation of LAP2β by dot blot during vorinostat pulse-chase experiment in Figure 3N (n = 9, 2-tailed t test).

(H) Supporting immunoblot of LAP2β OE for Figure 3O.

(I) Bioanalyzer tracing of genomic DNA following DamID labeling and DpnI restriction digest confirms activity of Dam-LAP2β fusion.

(J) qPCR of DamID labeled DNA from ASZ expressing indicated Dam constructs after 24hr serum withdrawal and vorinostat (10μM, 6 hour) or CRT (10μM, 2 hour) treatment (n = 4, ANOVA) with indicated primers.

Error bars represent standard error, error bars omitted when smaller than the width of associated data point symbol, ns = not significant, *p < 0.05, **p < 0.01, ***p < 0.001, ****p < 0.0001.
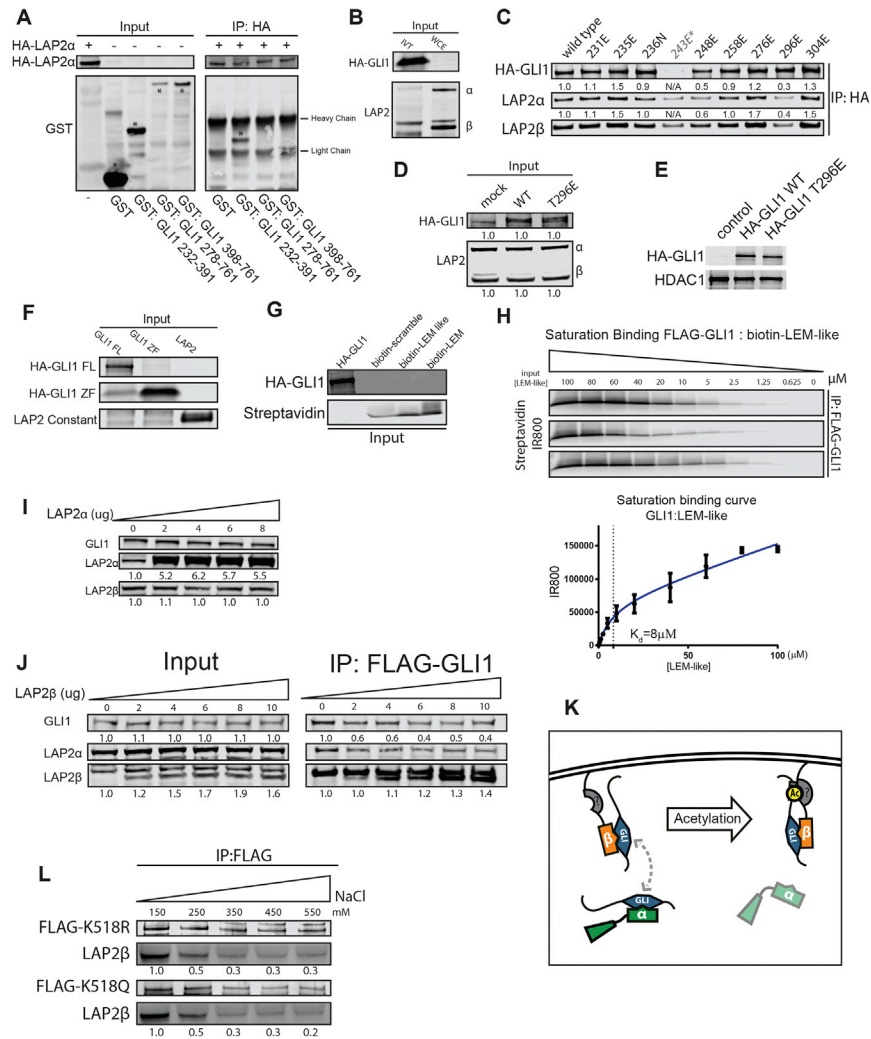
Figure S5. Related to Figure 4

(A) Co-IP of *in vitro translated* HA-LAP2α with recombinant GST-tagged fragments of GLI1. The fragment corresponding to full zinc-finger domain, but not fragment corresponding to zinc-finger domain missing 1st and 2nd zinc-finger IP with LAP2α.

(B) Input immunoblot associated with Figure 6A.

(C) Scanning mutagenesis of the zinc-fingers of GLI1 followed by co-IP of *in vitro translated* protein from WCE finds two mutants which disrupt LAP2 binding. Please not 243 did not express protein and was therefore disregarded. Associated with Figure 6B.

(D) Input immunoblot associated with Figure 6C.

(E) Immunoblot associated with Figure 6D.

(F) Input immunoblot associated with Figure 6E.

(G) Input immunoblot associated with Figure 6F.

(H) Saturation binding experiment in which limiting amounts of wheat cell *in vitro translated* FLAG-GLI1 co-IP following incubation over a gradient of biotinylated LEM-like domain. Quantitation below and saturation binding curve generated (n = 3, K_D = 8μM ± 8 SEM, r^2 = 0.92).

(I) Input immunoblot associated with Figure 6G.

(J) Reciprocal experiment as Figure 6G, in which GLI1 pulldown follows LAP2β OE. Exogenous LAP2β runs as subshifted band and correlates with loss of LAP2α-binding.

(K) Schematic illustrating LAP2 competitive binding mechanism with GLI1. LAP2α LEM-like domain (α, green) and LAP2β LEM-like domain (β, orange) bind to GLI1 zinc-finger domain (GLI, blue). GLI1 acetylation (Ac, yellow) creates secondary LAP2β binding site through an unidentified binding partner (?, gray).

(L) Wheat germ cell extract *in vitro translated* GLI1$_{K518R/Q}$ and LAP2β we co-IP followed by graded salt wash to assay for acetylation-dependent binding in a non-endogenous context.

Error bars represent standard error, error bars omitted when smaller than the width of associated data point symbol.
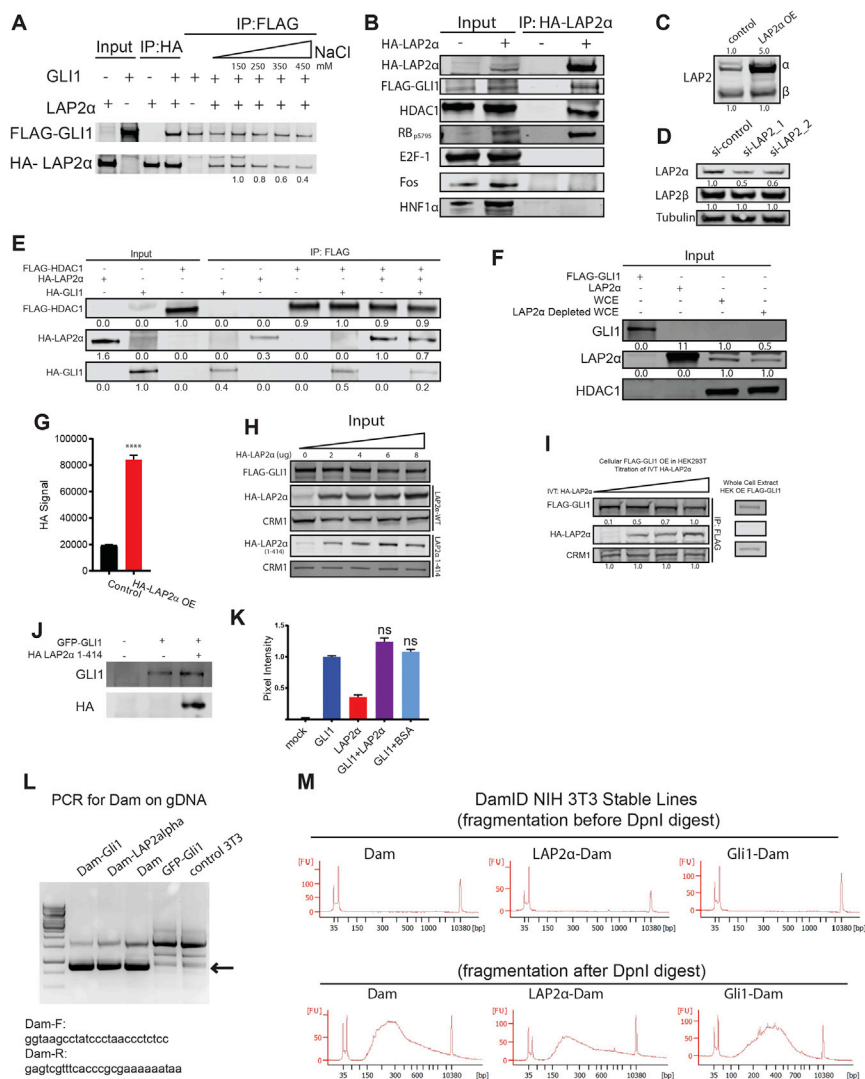
Figure S6. Related to Figure 5

(A) Extension of experiment in Figure 5A. Co-IP of LAP2α and GLI1 subjected to high salt wash gradient.

(B) Co-IP of HA-LAP2α co-transfected in HEK293T with FLAG-GLI1. Immunoblot for HA, FLAG, HDAC1, pRb (phosphorylation S795 antibody used due to reagent availability), E2F-1, Fos, and HNF1α.

(C) Immunoblot associated with Figure 5B demonstrates LAP2α but not LAP2β OE.

(D) Immunoblot associated with Figure 5C demonstrates specific LAP2α depletion.

(E) Immunoblot of co-IP of *in vitro* translated HDAC1, GLI1, and LAP2α.

(F) Input immunoblot associated with Figure 5E. Please note non-specific band above LAP2α band was not depleted with LAP2α-targeting siRNA and did not co-IP with GLI1.

(G) Quantification of HA by dot blot associated with vorinostat pulse-chase in Figure 5F (n = 9, ANOVA).

(H) Input immunoblot associated with Figure 5H.

(I) WCE of HEK293T transfected with FLAG-GLI1 incubated with a gradient of *in vitro translated* LAP2α followed by FLAG co-IP. Endogenous CRM1 does not compete with LAP2α for GLI1 binding *in vitro*.

(J) Immunoblots associated with cells from experiment in Figure 5I.

(K) Quantitation of signal intensity of EMSA in Figure 5K indicates no change with LAP2α addition (n = 7, ANOVA).

(L) PCR of genomic DNA from NIH 3T3 stableline expressing DamID constructs with indicated primers targeting Dam. Specific band, indicated by arrow, present in DamID stables but absent in controls. Associated with Figure 5L.

(M) Bioanalyzer traces of genomic DNA fragmentation by DpnI digestion confirms appropriate labeling with Dam constructs. Associated with Figure 5L.

Error bars represent standard error, error bars omitted when smaller than the width of associated data point symbol, ns = not significant, *p < 0.05, **p < 0.01, ***p < 0.001, ****p < 0.0001.